AGU PUBLICATIONS

JGR

Journal of Geophysical Research: Planets

RESEARCH ARTICLE
10.1002/2017JE005263

Special Section:
Investigations of the Bagnold Dune Field, Gale crater

Martian aeolian activity at the Bagnold Dunes, Gale Crater: The view from the surface and orbit

N. T. Bridges[1,2], R. Sullivan[3], C. E. Newman[4], S. Navarro[5], J. van Beek[6], R. C. Ewing[7], F. Ayoub[8], S. Silvestro[9,10], O. Gasnault[11], S. Le Mouélic[12], M. G. A. Lapotre[13], and W. Rapin[11,13]

[1]Applied Physics Laboratory, Laurel, Maryland, USA, [2]Deceased 26 April 2017, [3]Cornell Center for Astrophysics and Planetary Sciences, Cornell University, Ithaca, New York, USA, [4]Aeolis Research, Pasadena, California, USA, [5]Instituto Nacional de Técnica Aeroespacial, Torrejon de Ardoz, Spain, [6]Malin Space Science Systems, San Diego, California, USA, [7]Department of Geology and Geophysics, Texas A&M University, College Station, Texas, USA, [8]Jet Propulsion Laboratory, Pasadena, California, USA, [9]Osservatorio Astronomico Capodimonte, Naples, Italy, [10]SETI Institute, Carl Sagan Center, Mountain View, California, USA, [11]Centre National de la Recherche Scientifique, Institut de Recherche en Astrophysique et Planétologie, CNRS-Université Toulouse, Toulouse, France, [12]Laboratoire de Planétologie et Géodynamique de Nantes, CNRS, UMR 6112, Université de Nantes, Nantes, France, [13]California Institute of Technology, Pasadena, California, USA

Key Points:
- Dune activity observed on the surface of Mars
- Changes seen from Mars orbit and surface
- First estimate of wind threshold speeds on Mars in situ

Supporting Information:
- Supporting Information S1
- Figure S1
- Figure S2
- Figure S3
- Figure S4
- Figure S5
- Figure S6
- Figure S7
- Figure S8
- Figure S9
- Figure S10
- Figure S11
- Figure S12
- Figure S13
- Figure S14
- Figure S15
- Figure S16
- Figure S17
- Figure S18

Correspondence to:
C. E. Newman,
claire@aeolisresearch.com

Citation:
Bridges, N. T., et al. (2017), Martian aeolian activity at the Bagnold Dunes, Gale Crater: The view from the surface and orbit, *J. Geophys. Res. Planets, 122*, 2077–2110, doi:10.1002/2017JE005263.

Received 13 JAN 2017
Accepted 20 APR 2017
Accepted article online 30 MAY 2017
Published online 21 OCT 2017

© 2017. The Authors.
This is an open access article under the terms of the Creative Commons Attribution-NonCommercial-NoDerivs License, which permits use and distribution in any medium, provided the original work is properly cited, the use is non-commercial and no modifications or adaptations are made.

Abstract The first in situ investigation of an active dune field on another planetary surface occurred in 2015–2016 when the Mars Science Laboratory *Curiosity* rover investigated the Bagnold Dunes on Mars. High Resolution Imaging Science Experiment images show clear seasonal variations that are in good agreement with atmospheric model predictions of intra-annual sand flux and migration directions that together indicate that the campaign occurred during a period of low wind activity. *Curiosity* surface images show that limited changes nevertheless occurred, with movement of large grains, particularly on freshly exposed surfaces, two occurrences of secondary grain flow on the slip face of Namib Dune, and a slump on a freshly exposed surface of a large ripple. These changes are seen at Martian solar day (sol)-to-sol time scales. Grains on a rippled sand deposit and unconsolidated dump piles show limited movement of large grains over a few hours during which mean friction speeds are estimated at 0.3–0.4 m s^{-1}. Overall, the correlation between changes and peak Rover Environmental Monitoring Station (REMS) winds is moderate, with high wind events associated with changes in some cases, but not in others, suggesting that other factors are also at work. The distribution of REMS 1 Hz wind speeds shows a significant tail up to the current 20 m s^{-1} calibration limit, indicating that even higher speed winds occur. Nonaeolian triggering mechanisms are also possible. The low activity period at the dunes documented by *Curiosity* provides clues to processes that dominated in the Martian past under conditions of lower obliquity.

Plain Language Summary The modification of Martian sand dunes and nearby areas by the wind is monitored from the surface by the Curiosity rover and from orbit by the High Resolution Imaging Science Experiment camera. When the rover was at the dunes, changes were small but still showed moving grains and slumps. The results indicate that surface changes occur even in low activity periods, providing insight into past Martian climates.

1. Introduction

1.1. Background

Collocated, contemporaneous measurements of wind speed, sand flux, and bedform movement are necessary to understand the complexities of an aeolian sediment transport system. Measurements such as these are well established on Earth and serve to validate, refine, and test analytical and numerical models of aeolian sand transport and bedform dynamics [*Bagnold*, 1941; *Ould Ahmedou et al.*, 2007; *Mayaud et al.*, 2017]. On Mars, no single data set has been collected that incorporates all necessary measurements to completely characterize the aeolian sediment transport system. Although data collected from the Viking, Pathfinder, Mars Exploration Rover (MER), and Phoenix missions have contributed to this complex problem along with experimental data, models and orbital imagery, the conditions under which Martian sand is mobilized by the wind, are poorly understand. Now with recent data from the Mars Science Laboratory (MSL) *Curiosity* rover in the Bagnold Dune Field, supplemented with orbital data and climate models, our knowledge has

advanced considerably. Before discussing these results, we provide a brief discussion of the current understanding of conditions for sand movement on Earth and Mars.

1.2. Threshold Conditions of Terrestrial Dunes and Ripples

The wind speeds necessary to mobilize sand on Earth are fairly well established from wind tunnel, field, and theoretical studies. To initiate saltation from a flat granular bed, the surface shear stress (τ) from the wind must overcome forces that anchor sand to the surface, namely, the gravitational force (weight) and interparticle forces [*Greeley and Iversen*, 1985]. The lowest wind stress at which this occurs is referred to as the fluid threshold. The square root of shear stress divided by atmospheric density (ρ) has units of speed and is commonly referred to as the friction speed ($u*$). For turbulent conditions, wind speed at a given height (z) above the zero speed reference, or roughness height (z_0), varies logarithmically such that [*Prandtl*, 1935]

$$u(z) = (u^*/\kappa)\ln(z/z_0) = (\tau/\rho)^{0.5}\ln(z/z_0)/\kappa \quad (1)$$

where κ is the von Karman constant, equal to about 0.4. The shear stress can be considered as the downward momentum flux from the atmosphere that is transmitted to the surface. The threshold friction speed ($u*_t$) at which particles become detached from the surface and mobilized by the wind can be defined as [*Iversen et al.*, 1976; *White*, 1986]

$$u*_t = A(Re^*, f)\left(\left[\rho_p - \rho\right].gd/\rho\right]^{0.5} = \sim A(Re^*, f)\left(\rho_p gd/\rho\right)^{0.5} \quad (2)$$

where ρ_p is particle density, g is gravity, and d is particle diameter. A is a varying semiempirical coefficient which is dependent on the particle friction Reynolds number Re^* ($Re^* = u*_t d/\nu$, where ν is the kinematic viscosity, which is equal to the molecular viscosity divided by the atmospheric density) and interparticle forces (f). Once this fluid threshold is reached, grains are suspended or launched on ballistic saltation trajectories (depending on size and density), eventually colliding with the sand bed and thereby splashing more grains. Most of these grains are ejected at low speeds and can make one or several short hops along the surface in the reptation mode [*Anderson*, 1987; *Andreotti*, 2004]. When the sand density is much greater than the fluid density, such as on Earth and even more so on Mars, the transfer of momentum to the bed from collisions is more efficient than from fluid drag alone, such that saltation can be maintained below the fluid threshold value. The minimum speed at which saltation can occur from this process is termed the "impact threshold." Ratios of impact to fluid threshold are ~0.8 on Earth but only ~0.1 to 0.3 on Mars [*Kok*, 2010a, 2010b] (Figure 1a).

1.3. Threshold Conditions of Martian Dunes and Ripples

The study of Martian aeolian bedforms remains a less mature research field compared to that of dunes and ripples on Earth, although the plethora of high-quality images and other data from Mars missions, especially in the last decade, has substantially increased our understanding. Up until the Bagnold Dune Campaign [*Bridges and Ehlmann*, 2017; also see below], studies relied heavily on orbital imaging, mainly from the High Resolution Imaging Science Experiment (HiRISE) [*McEwen et al.*, 2007], and other remote sensing instruments. Martian sand dunes display the full spectrum of terrestrial classes [*Hayward et al.*, 2007], likely because the underlying physical parameters controlling morphology, namely, wind direction and intensity, and sand supply, are of sufficient strength and variability that the resulting forms are similar. This is despite, in comparison to Earth, an environment of 38% gravity, ~1.7% atmospheric density, lower frequency of winds above threshold, and a sand supply dominated by basalt instead of quartz.

Many Martian dunes are active, a characteristic that has been firmly established with high-resolution repeat HiRISE images [*Silvestro et al.*, 2010, 2011, 2013, 2016; *Chojnacki et al.*, 2011, 2014, 2015; *Hansen et al.*, 2011; *Bridges et al.*, 2007, 2012a, 2012b, 2013; *Geissler et al.*, 2013; *Fenton et al.*, 2014a, 2014b; *Cardinale et al.*, 2016; *Runyon et al.*, 2017]. Quantitatively, migration based on slip face advances and bulk dune movement ranges from 0.2 to 12 m yr^{-1}, with the Bagnold Dunes at the low end of this range (see below). Martian sand dune fluxes, computed by multiplying dune migration rate by dune crest height, or by taking the ratio of dune ripple displacement times ripple height to local dune height at the ripple position, range from 1 to 13 m^2 yr^{-1} [*Bridges et al.*, 2012b, *Ayoub et al.*, 2014; *Chojnacki et al.*, 2015]. These rates and fluxes are about 10–100 times less than typical dunes of equivalent height on Earth [*Bridges et al.*, 2012b]. Nevertheless, the activity of Martian dunes shows that sediment transport and resulting landscape modification through burial and abrasion may be the main geomorphic process in the current environment.

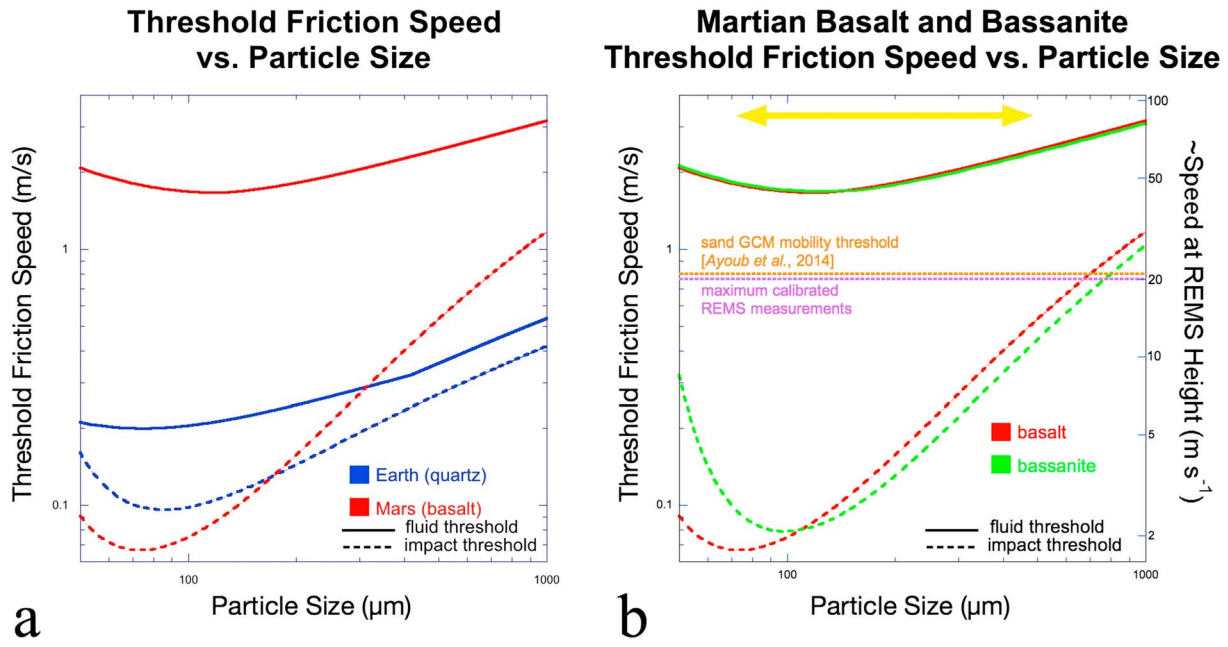

Figure 1. Particle threshold friction speed predictions on Earth and Mars. (a) A comparison of the predicted fluid and impact threshold for quartz on Earth and basalt on Mars. The fluid threshold was computed using the formulation of *Iversen and White* [1982] using particle densities of 2650 and 3000 kg m^{-3} for quartz and basalt, respectively. Earth temperature and pressure assumed at 273 K and 1 bar and for Mars at 209 K and 6.1 mb. The impact threshold curves were computed at the same conditions using the model of *Kok* [2010a, 2010b]. (b) Threshold curves for Mars only, with basalt and bassanite (2730 kg m^{-3}), materials that likely represent the dark sands and the most hydrated possible calcium sulfate that could make up the few bright particles, respectively, seen in the *Curiosity* images. The yellow arrow shows the range of grains sizes found at the Bagnold Dunes. The right *y* axis shows wind speeds that would be achieved at the 1.5 m height of the REMS wind sensor assuming a roughness height of 40 μm. The purple horizontal line represents the maximum speed at which REMS data can currently be retrieved with confidence. The sand mobility threshold of 0.01 Pa of *Ayoub et al.* [2014] is shown for an atmospheric density of 0.015 kg m^{-3}.

As many Martian dunes are active, the ripples on the surfaces of these dunes are also moving and at a rate that is linearly proportional to dune height. Such a relationship is consistent with flow acceleration and, given that dune ripple wavelength stays constant, an increasing sand flux up the dune stoss slope [*Bridges et al.*, 2012b]. Rates of ripple migration observed from HiRISE, and therefore biased to meter-scale and larger ripples that can be distinguished, are as great as 12 m yr^{-1}. Some dune ripples, such as those in Gale Crater, move longitudinally, reflecting the influence of two or more dominant winds [*Silvestro et al.*, 2016]. As seen from previous surface missions, only one episode of ripple movement has been documented in situ, with MER *Spirit* images showing a field of small ripples displaced by ~2 cm over 5 sols (Martian solar days) [*Sullivan et al.*, 2008]. Unfortunately, the MER payload lacked a wind sensor that could otherwise have been used to measure wind speeds associated with this event.

The threshold wind speed needed to mobilize sand on Mars has been evaluated in low-pressure wind tunnel investigations [*Greeley et al.*, 1974; *White*, 1979, 1986; *White et al.*, 1976; *Iversen and White*, 1982] and with theoretical, numerical, and semiempirical studies [*Claudin and Andreotti*, 2006; *Almeida et al.*, 2008; *Kok*, 2010a, 2010b; *Kok et al.*, 2012]. Considering just the balance between wind drag and normal force, the ~100 times lower density of the Martian atmosphere and ~1/3 gravity mean that wind speeds must be ~7 times greater than those on Earth for an equivalent density sand grain. Therefore, the likelihood of saltation occurring is correspondingly less. However, because of the high energetics of Martian saltation when it does occur, the ratio of momentum transfer from particle impacts into the bed relative to that from fluid drag is much greater than on Earth. This results in the Martian impact threshold being about 10 to 30% of the fluid threshold compared to about 80% on Earth [*Claudin and Andreotti*, 2006; *Kok and Renno*, 2009; *Kok*, 2010a, 2010b; *Kok et al.*, 2012] such that the impact thresholds on the two planets are comparable (Figure 1a). This indicates that although saltation may be hard to initiate on Mars, once begun it can be sustained more easily. This may explain the widespread movement of sand dunes and ripples seen from orbit. What threshold value to apply to Martian sand movement is uncertain, especially when assessing volumetric processes like dune migration. In comparing measured (from dune and ripple displacement) intra-annual sand flux variations in Nili Patera to

predicted sand fluxes using the Mars Weather Research and Forecasting (MarsWRF) climate model (see details below) [*Richardson et al.*, 2007; *Toigo et al.*, 2012; *Newman and Richardson*, 2015], it was found that the best match was achieved by setting a threshold shear stress of 0.01 Pa [*Ayoub et al.*, 2014]. This threshold should be considered an effective value to use in MarsWRF and other coarse-resolution models that do not capture the full turbulent wind spectrum. Converting this to a friction wind speed shows that it lies between the impact and fluid threshold wind speeds (Figure 1b), indicating that dune movement on Mars is driven by a combination of fluid lifting and impact splash. These values are also consistent with wind speeds as constrained from spatial heterogeneity of various mineral phases within the Bagnold Dune Field [*Lapotre et al.*, 2017]. Despite all of these orbital measurements, threshold wind speeds have never been measured in situ on Mars.

1.4. Motivation

Wind is the driving force for sand movement and, as elaborated upon above, it is well established that many bedforms on Mars are currently active despite an atmospheric density and threshold frequency that is lower than on Earth. On our planet, comparisons among wind speed, changes seen at the surface, and bedform movement are well established. These data serve to validate, refine, and test analytical and numerical models of aeolian bedform dynamics. Indeed, this interdependence of observations, measurements, and theory is fundamental for understanding any dynamic geologic process. On Mars, we presently only have pieces of this complex puzzle. Now with results from the Bagnold Dune Campaign in hand, and an extensive record of HiRISE images, this paper is motivated to address this shortcoming.

The Bagnold Dune Campaign, during which the ground truth measurements herein were obtained, could not be constrained to any particular time of the Martian year given that the *Curiosity* mission is paced by operational requirements and programmatic directives that dictate the overall traverse route and timing. Therefore, not by design but rather because of many uncontrollable factors, the campaign was, as we will show, conducted at a time of year at which aeolian activity was low. Therefore, the full suite of potential dynamic processes that occur on Mars could not be evaluated, including the highest energy events that likely do the most geomorphic work. Although such an evaluation awaits future data and studies, we will show that the results obtained here are representative of the most common mode of aeolian activity on Mars and therefore provide insight into other areas of the planet and past climates.

We begin with a discussion of methods used to evaluate aeolian processes in the Bagnold Dune field, namely, the MarsWRF atmospheric model, change detection with HiRISE images, and *Curiosity*'s investigation of the Bagnold Dunes. The results of these three methodologies are then presented, each of which indicates a minor level of surface aeolian activity at the time of the Campaign. We then evaluate the implications for the processes that were observed, both as they inform upon particle mobility on Mars, and aeolian geology elsewhere on the planet. We argue that limited aeolian activity as observed is common on Mars and likely dominates in periods of lower obliquity.

2. Methods

2.1. MarsWRF Model

MarsWRF is the Mars version of the planetWRF model [*Richardson et al.*, 2007; *Toigo et al.*, 2012] and serves as a global-to-mesoscale model of the Martian atmosphere. The model includes radiative transfer through a dusty CO_2 atmosphere, heat and momentum exchange, CO_2 frost condensation and sublimation, and horizontal and vertical eddy mixing at scales smaller than the model's grid separation. The model includes topography and surface roughness maps derived from the Mars Orbiter Laser Altimeter [*Smith et al.*, 2001], and surface thermal inertia and albedo maps from Thermal Emission Spectrometer data [*Christensen et al.*, 2001].

For this work, and that in *Newman et al.* [2017], the global model (domain 1) was run at 2° horizontal resolution, with five higher resolution nests (domains 2–6) embedded within each other and centered on Gale Crater. Each nest has a threefold increase in resolution over its parent, resulting in a grid spacing of ~490 m in the innermost nest, which sits inside Gale centered on the Bagnold Dune field. At this scale, dune topography cannot be resolved. Hence, the results provide gross averages of sand transport that can be compared to HiRISE and surface measurements. To model the long-term wind regime, nested simulations were performed every 30° of areocentric solar longitude (L_s) to capture the seasonal cycle. Each nested simulation lasted up to 9 sols, although the first 2 sols were discarded (to avoid spin-up effects). Near-surface wind

vectors, air density (ρ), and wind shear stress (τ) were output every minute. 5 to 7 sols were then used from each period, depending on the fraction of the year spent in each 30° L_s "season," and were combined to provide a proxy for the annual wind field. The sand "drift potential," proportional to flux, was computed at each point as $u*^2(u* - u*_t)$ [*Fryberger and Dean*, 1979; *Tsoar*, 2001] and compiled into wind rose diagrams that showed the predicted relative flux as a function of wind azimuth. This was done for two conditions, one assuming that the threshold shear stress was 0 and another using the 0.01 Pa value from *Ayoub et al.* [2014] which, as discussed above, is likely the appropriate threshold to use when predicting fluxes based on mesoscale model winds. Wind speeds were also extrapolated down to the 1.5 m elevation of the Rover Environmental Monitoring Station (REMS) wind sensor, following the procedure described in *Newman et al.* [2017]. In this paper, the innermost nest grid point closest to the location of the Bagnold Dune Campaign, at 137.37°E, 4.69°S, was used.

2.2. HiRISE-Derived Change Detection

HiRISE has been acquiring data in its primary science orbit of Mars since late 2006. With a pixel scale as fine as 25 cm/pixel, it is the highest resolution orbital imaging system ever to investigate Mars. It has a field of view of 20,000 pixels (~5 km) wide and variable length that typically ranges from 5 to 25 km. The HiRISE focal plane consists of 14 charge couple device arrays that sum signal through time delay integration in push-broom mode. Over the entire field of width, 10 CCDs collect light over a wavelength range of 570–830 nm ("red"). In the center 20%, two sets of two CCDs are sensitive to wavelengths $<$588 nm ("blue-green") and $>$790 nm ("infrared") to provide color information [*McEwen et al.*, 2007]. With the ability to target any location within ±30° from the nadir ground track, two images of the same location can be used to make a digital elevation model (DEM) derived from stereo match points with a vertical precision of tens of centimeters [*Kirk et al.*, 2008]. From the DEM and the original image, two orthorectified image products are made that can be used as master products to orthorectify later change detection images. As of this writing, HiRISE has taken over 48,000 images of Mars.

On Earth, measuring wind speed, flux, ripple displacements, and other parameters on individual dunes and within fields requires networks of anemometers, sand traps, cameras, and other sensors, an intensive and expensive exercise that, by its nature, cannot be done with complete spatial coverage. Ironically, satellite and aerial tracking of dune changes on Earth are inferior to those obtainable with HiRISE due to limitations in resolution (civilian satellite resolutions are coarser than HiRISE's 25 cm/pixel) and the much larger size of many Martian ripples [*Vaz and Silvestro*, 2014; *Lapotre et al.*, 2016], which makes them easier to track than their terrestrial counterparts. Using change detection software on orthorectified images with corresponding DEM topography, dune ripple displacements can be tracked across entire dune fields, with the positions relative to local terrain measured with subpixel accuracy. In essence, such detailed analyses serve as proxy surface weather stations from which the response to and intensity of the wind can be gauged.

The change detection software we use is COSI-Corr (Co-registration of Optically Sensed Images and Correlation) [*Leprince et al.*, 2007]. The COSI-Corr methodology allows for automatic and precise orthorectification, co-registration, and subpixel correlation of push broom satellite and aerial images. Orthorectified images are resampled to a common grid; that is, each pixel is projected onto a specific geographic location. Relative displacement between the image pairs is found from the phase difference in their Fourier transform along column (vertical) and row (horizontal) axes. COSI-Corr has been successfully used to measure diverse tectonic and geomorphic processes, including coseismic deformation, ice flow, landslide, and sand dune migration on Earth [*Avouac et al.*, 2006; *Leprince et al.*, 2007; *Vermeesch and Drake*, 2008; *Necsoiu et al.*, 2009] and has also been applied to sand dunes on Mars [*Bridges et al.*, 2012b; *Ayoub et al.*, 2014].

Because of the intense scientific interest in Gale Crater, it has been extensively imaged by HiRISE. As of this writing, there have been 18 images acquired of the region investigated during the Bagnold Dune Campaign (Table 1). These dunes are the focus of the HiRISE analysis in this paper because they are most applicable to addressing changes seen with *Curiosity* (for a broader study of the Gale Crater dunes see *Silvestro et al.* [2013, 2016; *Day and Kocurek*, 2016]). Here we abbreviate the image IDs with the designation "*Tx*" where *T* refers to time and *x* is a number that starts with the first image acquired, PSP_009149_1750 on 9 July 2008. The designation *Sy* is added if the image is part of a stereo pair, with *y* being a number 1 or 2 to refer to whether the image is the earlier or latter of the image pair. Although the dunes within Gale Crater have been shown to be active [*Silvestro et al.*, 2013, 2016], their displacements are less and the moving ripples smaller than in areas such as Nili Patera that have also been extensively studied [*Silvestro et al.*, 2010; *Bridges et al.*, 2012b; *Ayoub et al.*, 2014]. Therefore,

Journal of Geophysical Research: Planets

10.1002/2017JE005263

Table 1. HiRISE Images of the Bagnold Dunes[a]

Image	Type	Roll Angle (°)	MY	L_s (°)	Date	ΔT	Red LUT	Ortho Master	ΔT	Corr to	ΔT	Results
PSP_009149_1750	T1/S1	−12.9	29	96.3	9/7/08	0	dark	NA	NA	NA	NA	
PSP_009294_1750	T1/S2	2.2	29	101.3	20/7/08	11	dark	NA	NA	NA	NA	
ESP_018854_1755	T2/S1	5.5	30	61.1	4/8/10	756	dark	NA	NA	NA	NA	
ESP_018920_1755	T2/S2	−18.1	30	130.6	9/8/10	761	medium-dark	NA	NA	NA	NA	
ESP_021610_1755	T3	−26.0	30	249.7	7/3/11	971	medium-bright	NA	NA	NA	NA	
ESP_033649_1750	T4	−2.4	32	29.1	30/9/13	1909	medium-dark	T2/S1	1153	T2/S1	1153	displacements
								T9/S1	−439	NA	NA	
ESP_035772_1755	T5	−15.8	32	102.3	14/3/14	2074	dark	NA	NA	NA	NA	
ESP_035917_1755	T6	3.5	32	107.4	26/3/14	2086	very dark	T9/S1	−274	T4 orthored to T9/S1	177	*no displacements*
ESP_036194_1755	T7	−16.9	32	117.4	16/4/14	2107	medium-dark	NA	NA	NA	NA	
ESP_037117_1755	T8	−13.0	32	152.5	27/6/14	2179	very dark	T9/S1	−241	T4 orthored to T9/S1	270	*no displacements*
ESP_039280_1755	T9/S1	5.4	32	251.6	13/12/14	2348	dark	x	NA	T4 orthored to T9/S1	439	*no displacements*
ESP_040770_1755	T9/S2	24.1	32	322.2	8/4/15	2464	dark	x	NA	T9/S1	116	minor displacements
ESP_042682_1755	T10	−1.9	33	36.8	4/9/15	2613	dark	T9/S1	265	T4 orthored to T9/S1	704	displacements
ESP_043539_1755	T11	28.0	33	66.3	10/11/15	2680	dark	T9/S2	216	T9/S2	216	*no displacements*
ESP_044172_1755	T12	22.4	33	87.9	29/12/15	2729	NA	T9/S2	265	T9/S2	265	*no displacements*
ESP_045293_1755	T13	21.1	33	127.7	25/3/16	2816	dark	T9/S2	352	T9/S2	352	*no displacements*
ESP_046137_1755	T14	−12.1	33	160.8	30/5/16	2882	medium-dark	T9/S1	534	T10	269	minor displacements
ESP_047416_1755	T15	−0.6	33	218.2	7/9/16	2982	medium-dark	T9/S1	634	T10	369	

[a]Notes: MY = Mars year; L_s is the areocentric longitude around the Sun; ΔT in column 7 is the elapsed time in Earth days from the first image; LUT is the 14 to 8 bit look-up table used onboard MRO to generate the HiRISE image; ortho master is the orthorectified image from a digital elevation model that the slave image was registered to; ΔT in column 10 is the time in Earth days between the acquisition of the ortho master and slave; "Corr to" is the previous image that this image was correlated to; ΔT in column 12 is the day in Earth days between the correlations. Further details are described in the text. For more details on HiRISE, see *McEwen et al.* [2007] and for the COSI-Corr correlation procedure *Leprince et al.* [2007], *Bridges et al.* [2012b], and *Ayoub et al.* [2014].

quantifying displacements on the Bagnold Dunes from orbit is challenging. In addition, only a subset of these images was applicable for measuring dune ripple displacements with COSI-Corr because of the following: (1) Some images did not have corresponding DEM coverage for the area of interest close in time to image acquisition (images *T*1/*S*1 and *T*1/*S*2). (2) One image, *T*3, was acquired using an onboard 14 to 8 bit look-up table (LUT), designated "medium-bright," that is best suited for providing high radiometric precision on bright bedrock and not dark dunes [*McEwen et al.*, 2007] so sand ripples could not be easily distinguished. (3) Images *T*5 and *T*6 were acquired just 12 days apart. Image *T*6 had a "very dark" LUT that is preferable to the "dark" LUT used in *T*5. Therefore, *T*6 was used and *T*5 was not. (4) In correlating *T*4 to later images, *T*7 was skipped because it had a brighter LUT than the later *T*8 and *T*9*S*1. Because no changes were found between *T*8 or *T*9*S*1 and *T*4, *T*7 was left unexamined. (Had changes been found between *T*8 and *T*4, *T*7 would have been correlated to *T*4 to identify displacements at a finer temporal scale.)

Despite these constraints, the data were sufficient to evaluate overall displacements over time scales longer than a Mars year. This involved correlating images *T*2/*S*1 to *T*4 and *T*10 to *T*4. These provided a record over 1153 and 704 Earth days (nearly two Mars years and just over one Mars year, respectively). Comparing orthoimages *T*9*S*2 to *T*9*S*1 over 116 days provided displacements in the high flux season (Mars year (MY) 32, L_s 253–322°) as predicted by MarsWRF and seasonal sand fluxes in Nili Patera [*Ayoub et al.*, 2014], see also sections 3.1 and 3.2. Finally, comparing displacements between *T*10 (L_s = 37°) and later images showed either a lack of changes (*T*11–13) or very few displacements (*T*14) in the low flux season that corresponded to the time period of the Bagnold Dune Campaign.

The COSI-Corr procedures used here are similar to those described in detail in past studies [*Leprince et al.*, 2007; *Bridges et al.*, 2012b; *Ayoub et al.*, 2014] and the COSI-Corr users' guide [*Ayoub et al.*, 2015]. In brief, bedrock ground control points (GCPs) identified in raw ("slave") images of interest were tied to those in a corresponding stereo-derived orthoimage ("master") that was closest in time and roll angle. Using the COSI-Corr frequency correlator and a 256 × 256 pixel sliding window, these GCPs were refined with resulting subpixel precision. The optimized GCPs, orthoimage, and DEM were then used in COSI-Corr to convert the raw image into a resampled (25 cm/pixel) product precisely registered on the bedrock to the master. Orthoimages with common grids were then correlated with each other using the COSI-Corr frequency correlator initially with a 128 × 128 and finally with a 32 × 32 pixel window with a sliding step of 8 pixels. This produced average N-S and E-W displacement maps with a resolution dictated by the sliding window size of 8 pixels (2 m). The correlation products were then cleaned by removing noise, "destriping" variations along the ground track azimuth resulting from CCD misalignment and jitter, and, in some cases, applying a fifth-degree polynomial fit to "detrend" along-track sinusoidal variations [*Ayoub et al.*, 2015]. After such processing, the bedrock misregistration was generally less than 0.1 pixel. Next, regions of interest were made around dunes and sand patches to determine displacements. Because of the small size and low albedo of the ripples, correlation noise prevented measurement of displacements less than about a meter. However, displacement vectors >1 m within each 2 m^2 window were tabulated and plotted as a function of size and azimuth on rose diagrams. Displacement magnitudes were made into maps and overlaid on the dunes. As will be shown later in the paper, a dominance of displacements to the southwest that is fairly consistent with the predicted overall dune transport direction predicted by MarsWRF, and the location of the highest displacements, give confidence that the results are robust and provide information on seasonal variations in sand activity in the Bagnold Dune Field.

2.3. MSL Instruments and the Bagnold Dune Campaign

2.3.1. Instruments

The *Curiosity* payload is better suited for studying current aeolian conditions on Mars than previous landers or rovers. We focus here on the imaging and anemometry instruments that are relevant for change detection studies. The rover mast science cameras, Mast Camera (Mastcam) and the Chemical Camera (ChemCam) Remote Micro-Imager (RMI), provide images of different coverage and spatial scale. Mastcam acquires stereo color imaging with two cameras, M34 (left eye, 34 mm focal length) and M100 (right eye, 100 mm focal length), with pixel scales of 220 and 74 μrad, respectively [*Malin et al.*, 2010]. RMI, at 19.6 μrad/pixel [*Maurice et al.*, 2012; *Le Mouélic et al.*, 2015], is the highest resolution remote imager ever put on a planetary surface in terms of pixel sampling, exceeded only in spatial scale by microscopic imagers placed close to rocks and soils. With radiometric processing to correct for nonlinearity and flat field, fine details can be discerned [*Le Mouélic et al.*, 2015].

The Rover Environmental Monitoring Station (REMS) measures wind speed and direction, pressure, relative humidity, air temperature, ground temperature, and ultraviolet radiation. Routine observations typically involve 1 Hz sampling for the first 5 min every Mars hour, but this can be augmented with multiple extended blocks (EBs) of 1 h duration at 1 Hz that are commonly linked together in groupings of up to 5 h (limited by the REMS buffer capacity of 63 5 min blocks) [*Gómez-Elvira et al.*, 2012, 2014; *Newman et al.*, 2017] (henceforth in this paper, the term "hour" refers to a Mars hour, which is 1/24th of a sol). Single EBs are generally timed near sunrise to capture rapid diurnal changes in relative humidity and close to local noon to capture the period of peak solar radiation and to monitor the meteorological impact of convective vortices (which tend to occur most frequently in the early afternoon). With no other constraints, the other EBs are spaced 6 h apart, shifting 1 h earlier each sol (covering the diurnal cycle in 1 h blocks every 6 sols), with additional lower-priority 3 h blocks that are repeated for 3 sols before shifting 3 h earlier (covering the diurnal cycle in 3 h blocks every 24 sols). However, EBs can also be timed to correspond to periods of specific interest during science campaigns, such as for change detection imaging. Unfortunately, each of the two REMS sensor booms extending from the remote-sensing mast suffered damage during landing, probably due to debris ejected from the surface by retrorockets [*Gómez-Elvira et al.*, 2014; *Newman et al.*, 2017]. The side-/rear-facing boom was sufficiently damaged that it could not be used for wind retrievals, leaving only the front-facing boom, on which one out of the three sensors was also damaged. As both booms are mounted on the thick remote sensing mast (RSM), flow is highly perturbed when it has to pass around the RSM before reaching the boom. With only the front-facing boom available, this means that winds coming from the hemisphere to the rear of the rover cannot be retrieved with good accuracy in terms of direction, and no "rear" wind speeds can be retrieved at all. Despite these difficulties, when the rover is properly oriented, 1 Hz measurements are retrieved with a directional accuracy of ±15° and wind speeds up to the calibration limit of 20 m s^{-1} of ±20% [*Newman et al.*, 2017]. At temperatures below ~210 K, noise in the wind sensor electronics overwhelms signal that might be extracted. During the Bagnold Dune Campaign, which overlapped the coldest time of year, this constraint resulted in reliable REMS data between ~08:00 and 24:00 from L_s = 67–75° (wind characterization campaign and ripple crossing near High Dune), ~09:00 and 22:00 from L_s = 82–91° (in front of Namib Dune), and between ~08:00 and 21:00 from L_s 92–104° (Solitaire and Hebron). Further details of the retrieval scheme and filtering of results to remove spurious data are described in *Newman et al.* [2017].

2.3.2. Campaign Methodology

Prior to *Curiosity*'s landing, it was recognized that the nominal drive path required passing through a sand dune field that had previously been shown as active [*Silvestro et al.*, 2013]. Although the overarching strategic goal of MSL was (and is) to ascend Mount Sharp (Aeolis Mons) to assess past environments [*Grotzinger et al.*, 2015], the mission team recognized that an investigation of the first active dune field on another planetary surface could be achieved with minimal impact. With a sophisticated suite of instruments, several investigations were planned, including those for change detection using the imaging payload and REMS environmental package.

Details of the MSL Bagnold Dune campaign are described in *Bridges and Ehlmann* [2017], and the REMS wind measurements in particular in *Newman et al.* [2017]. The composition and characteristics of the grains composing the Bagnold Dunes and nearby sands are reported in several other papers [*Cousin et al.*, 2017; *Ehlmann et al.*, 2017; *Ewing et al.*, 2017; *Lapotre et al.*, 2017; *O'Connell-Cooper et al.*, 2017; *Sullivan and Kok*, 2017; all in the Bagnold Dune Field Special Issue], the details of which are relevant to change detections in terms of the size and density of the grains. In these studies, it is found that sand composing the Bagnold Dunes is generally less than 250 μm in size, with a few grains larger than 500 μm. Compositions are similar to mafic soils analyzed along the traverse prior to arriving at the dune field, but with greater amounts of silicon, magnesium, iron, and nickel and lower hydrogen, sulfur, and chlorine. Some grains are bright and may represent local calcium sulfate vein fragments, although these sands were not analyzed independently so their compositions cannot be confirmed. Given the measured size range and density differences between mafic (~3000 kg m^{-3}) and calcium sulfate (2730 kg m^{-3} for bassanite [*Rapin et al.*, 2016]), potential threshold winds to detach the sand grains from the surface vary by factors of about 1.5 to 5 depending on whether fluid or impact threshold is assumed (Figure 1b).

The following is a brief overview highlighting where and how change detection experiments were conducted. *Curiosity*'s path through the dune field started with an approach from the north, with three stops, on sols (Mars days elapsed since landing) 1162, 1167, and 1168 in which the rover parked in roughly equally separated azimuths (314.2°, 193.1°, and 75.7°, respectively) to assess the local wind field and determine the ideal rover orientation in which to measure the strongest daytime winds later in the campaign (Figure 2).

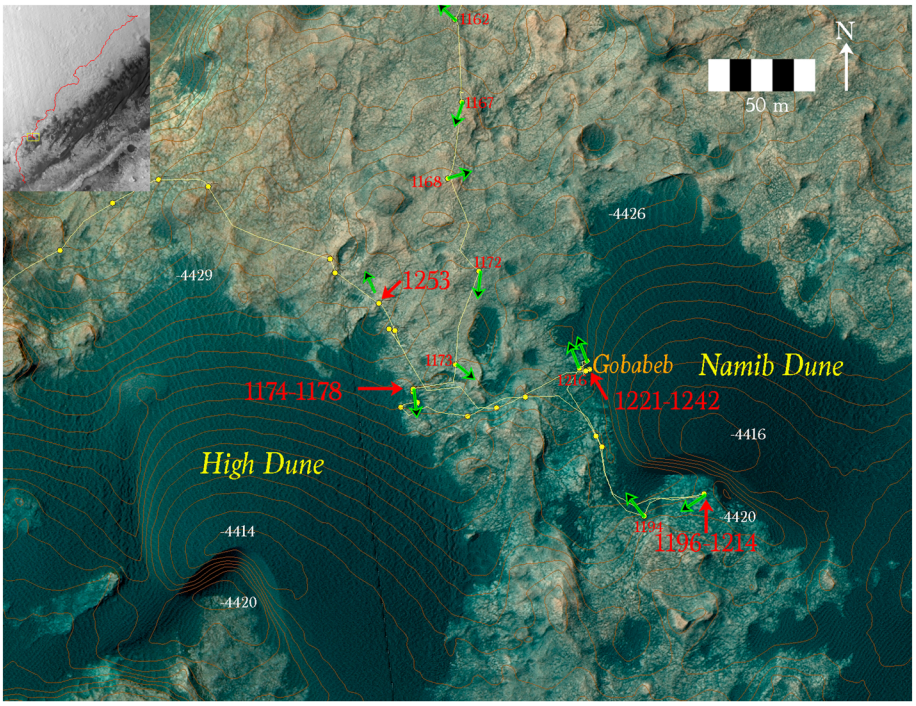

Figure 2. *Curiosity*'s traverse in the Bagnold Dune Campaign overlain on a color HiRISE image. Rover stops are shown as yellow dots, with the sols (Martian days since landing) of the most important stops for this work labeled with red numbers. The largest red numbers show the sols where change detection activities occurred. The green arrows show the rover heading at various stops. Elevation contours are shown as brown lines with 1 m spacing and elevation labels are white. The inset at top left shows a CTX mosaic with the entire *Curiosity* traverse path from landing to 4 April 2017 (from Google Earth), with the yellow box outlining the location of the main figure.

Daytime winds were prioritized both because intrasol change detection experiments occurred during daylight hours and because temperatures were too cold to measure winds over much of the night. From these data, it was determined that the highest speed daytime winds at this season, southern fall to winter, were from the northwest [*Newman et al.*, 2017].

The general approach for change detection observations was simple: image the same area of potential wind-induced surface modification over time and, when possible, have gaps between repeat images spanned by REMS extended blocks (Tables 2 and 3a). Because of constraints on data buffering, a bridged record was only possible between images acquired no more than a few hours apart on a single sol. Nevertheless, given that peak daytime winds commonly occur between 11:30 and 18:00 [*Newman et al.*, 2017], the coverage of blocks was sometimes sufficient that the likely highest daytime wind activity times could be assessed between images taken on different sols. Images generally were Mastcam M100, with some M34 for stereo and, in two cases, RMI (Table 2) (many other Mastcam and RMI images were taken for purposes besides change detection). Most Mastcam images were losslessly compressed to best preserve details in dark sand targets. Some images were initially downlinked as thumbnails and only retransmitted later at full resolution if they could better constrain the timing of changes identified between images spaced more widely in time. Over multiple sols, it was desirable to obtain repeat imaging near the same local true solar time (LTST) so that similar lighting angles would make changes easier to recognize. However, some repeat imaging was obtained at several times of day to gauge changes over a period of hours. In these cases, REMS EBs were scheduled to provide continuous wind monitoring between images. Especially for close images with nearly equivalent lighting geometry, there was high confidence that similar looking displaced grains (approximate size, shape, and tone) between images were indeed the same particles and grains that appeared or disappeared were transported in or out, respectively, of the scene. However, in other cases where images were of pure sand deposits (so not bedrock below) and times of day were different or the view was more distal (such as the Namib dune slipface), the possibility exists that some changes could be spoofed by specular reflection off grain microfacets.

Table 2. MSL Change Detection Images During the Bagnold Dune Campaign[a]

Image Type (Hor. × Vert.)	Target Distance (m)	Pixel Scale (mm)	Rover Heading (° from N)	Image Azimuth (° from N)	Date	L_s (deg)	Sol	LMST	LTST	Image ID	Compression	Abbreviation	Figures
					Ripple Crossing Near High Dune								
3 × 3 L0_R0	2.91	0.22, 0.64	176.5	191.1	25/11/15	72.8	1174	14:08	14:16	MCAM05325	lossless	rc1	10, S2
					27/11/15	73.6	1176	14:55	15:04	MCAM05328	lossless	rc2	
					28/11/15	74.1	1177	13:16	13:25	MCAM05335	lossless	rc3	
					29/11/16	74.5	1178	14:01	14:10	MCAM05336	lossless	rc4	
					Namib Dune Lee Face Region								
					Near Rover Imaging								
					Distributed Near Field								
4 × 1 R0	2.58	0.19	235.5	259.8	20/12/15	83.7	1198	12:30	12:45	MCAM05454	lossless	Nnf1	12, S3a–S3d
					22/12/15	84.6	1200	12:25	12:38	MCAM05498	lossless	Nnf2	
					23/12/15	85	1201	12:04	12:18	MCAM05505	lossless	Nnf3	
					24/12/15	85.4	1202	11:21	11:34	MCAM05512	lossless	Nnf4	
								13:55	14:08	MCAM05535	lossless	Nnf5	
					25/12/15	85.9	1203	14:37	14:51	MCAM05539	lossless	Nnf6	
								16:17	16:30	MCAM05544	lossless	Nnf7	
					Sol 1204 Turn								
9 × 1 R0	2.58	0.19	235.2	265.7	28/12/15	87.2	1206	11:41	11:55	MCAM05396	lossless	Nnf8	
								16:06	16:20	MCAM05401	lossless	Nnf9	
					29/12/15	87.6	1207	07:58	08:12	MCAM05408	lossless	Nnf10	
					1/1/16	89.0	1210	11:51	12:06	MCAM05426	lossless	Nnf11	
								13:06	13:20	MCAM05431	lossless	Nnf12	
								14:35	14:49	MCAM05444	lossless	Nnf13	
								16:05	16:19	MCAM05434	lossless	Nnf14	
								17:07	17:21	MCAM05447	lossless	Nnf15	
					2/1/16	89.4	1211	07:58	08:12	MCAM05441	lossless	Nnf16	
4 × 1 R0				259.8	5/1/16	90.7	1214	12:42	12:57	MCAM05521	lossless	Nnf17	
					Clast Survey								
R0	2.77	0.20	235.5	356.1	20/12/15	83.7	1198	12:42	12:56	MCAM05492	85	Ncs1	12, S3e
					Sol 1204 Turn								
	2.72	0.20	235.2	355.6	26/12/15	86.3	1204	16:12	16:25	MCAM05551	85	Ncs3	
					28/12/15	87.2	1206	11:35	11:51	MCAM05394	lossless	Ncs4	
								16:00	16:15	MCAM05399	lossless	Ncs5	
					29/12/15	87.6	1207	07:52	08:07	MCAM05406	lossless	Ncs6	
					1/1/16	89.0	1210	11:46	12:01	MCAM05424	lossless	Ncs7	
								13:00	13:16	MCAM05429	lossless	Ncs8	
								14:30	14:46	MCAM05442	lossless	Ncs9	
								16:00	16:16	MCAM05432	lossless	Ncs10	
								17:00	17:17	MCAM05445	lossless	Ncs11	
					2/1/16		1211	07:52	08:07	MCAM05439	lossless	Ncs12	
					5/1/16		1214	12:33	12:50	MCAM05519	lossless	Ncs13	
					Lee Face Context Imaging								
360° mosaic 20 × 10 L0	15.08	3.32	235.5	NA	18/12/15	82.8	1197	14:50	15:03	MCAM05456	variable	Nctx1	
Slip face 12 × 2 L0	15.08	3.32		82.6	22/12/15	84.6	1200	12:16	12:32	MCAM05496	lossless	Nctx2	
					23/12/15	85.0	1201	11:57	12:13	MCAM05504	lossless	Nctx3	3
					24/12/15	85.4	1202	11:13	11:30	MCAM05511	lossless	Nctx4	

AGU Journal of Geophysical Research: Planets

10.1002/2017JE005263

Journal of Geophysical Research: Planets

10.1002/2017JE005263

Table 2. (continued)

Image Type (Hor. × Vert.)	Target Distance (m)	Pixel Scale (mm)	Rover Heading (° from N)	Image Azimuth (° from N)	Date	L_S (deg)	Sol	LMST	LTST	Image ID	Compression	Abbreviation	Figures
								13:47	14:04	MCAM05534	lossless	Nctx5	
Eastern slip face 6 × 2 L0	15.03	3.31		295.1	25/12/15	85.9	1203	14:43	14:57	MCAM05541	lossless	Nctx6	
Sol 1204 Turn													
Slip face 12 × 2 L0	15.08	3.32	235.2	42.6	5/1/16	90.7	1214	12:35	12:53	MCAM05520	lossless	Nctx7	
Lee Face Focused Imaging													
Lower Eastern													
2 × 3 L0_R0	15.04	1.11, 3.31	235.5	42.9	20/12/15	83.7	1198	12:32	12:47	MCAM05462	lossless	NIE1	
					22/12/15	84.6	1200	12:26	12:40	MCAM05499	lossless	NIE2	
					23/12/15	85	1201	12:05	12:20	MCAM05506	lossless	NIE3	
					24/12/15	85.4	1202	11:21	11:36	MCAM05513	lossless	NIE4	
								13:55	14:10	MCAM05536	lossless	NIE5	
					25/12/15	85.9	1203	14:38	14:53	MCAM05540	lossless	NIE6	
								16:18	16:33	MCAM05545	lossless	NIE7	
Sol 1204 Turn													
2 × 4 R0	15.14	1.12	235.2	42.2	28/12/15	87.2	1206	11:37	11:52	MCAM05395	lossless	NIE8	
								16:01	16:18	MCAM05400	lossless	NIE9	
					29/12/15	87.6	1207	07:53	08:08	MCAM05407	lossless	NIE10	
					1/1/16	89	1210	11:48	12:03	MCAM05425	lossless	NIE11	
								13:02	13:18	MCAM05430	lossless	NIE12	
								14:32	14:48	MCAM05443	lossless	NIE13	
								16:01	16:18	MCAM05433	lossless	NIE14	
								17:02	17:19	MCAM05446	lossless	NIE15	
					2/1/16	89.4	1211	07:53	08:10	MCAM05440	lossless	NIE16	
2 × 3 L0_R0		1.12, 3.33		42.9	5/1/16	90.7	1214	12:44	13:00	MCAM05522	lossless	NIE17	
Central (Mastcam)													
3 × 6 L0_R0	15.09	1.12, 3.32	235.5	10.6	20/12/15	83.7	1198	12:35	12:52	MCAM05491	lossless	NC1	13, S4a, S4c
					22/12/15	84.6	1200	12:27	12:40	MCAM05500	lossless	NC2	
					24/12/15	85.4	1202	11:23	11:39	MCAM05514	lossless	NC3	
								13:57	14:10	MCAM05537	lossless	NC4	
Sol 1204 Turn													
	15.04	1.11, 3.31	235.2	10.8	5/1/16	90.7	1214	12:45	13:00	MCAM05523	lossless	NC5	
Upper Central (RMI)													
1 × 1	15.00	0.29	235.2	12.3	20/12/15	83.7	1198	12:20	12:37	CCAM01198	ICER 6, MINLOSS 2	NuC1	
5 × 1				11.6	21/12/15	84.1	1199	11:43	12:00	CCAM04198	ICER 6, MINLOSS 2	NuC2	
10 × 1				9.8	22/12/15	84.6	1200	12:46	12:59	CCAM01200	ICER 6, MINLOSS 2	NuC3	S4b
					23/12/15	85	1201	11:34	11:47	CCAM04200	ICER 6, MINLOSS 2	NuC4	
5 × 1				11.6	24/12/15	85.4	1202	10:54	11:07	CCAM04201	ICER 6, MINLOSS 2	NuC5	
								13:27	13:40	CCAM01202	ICER 6, MINLOSS 2	NuC6	
West Central													
L0_R0	15.11	1.12, 3.32	235.5	358.8	23/12/15	85	1201	14:21	14:36	MCAM05508	lossless	NwC1	
					24/12/15	85.4	1202	11:28	11:42	MCAM05515	lossless	NwC2	
								14:02	14:16	MCAM05538	lossless	NwC3	

Journal of Geophysical Research: Planets

10.1002/2017JE005263

Table 2. (continued)

Image Type (Hor. × Vert.)	Target Distance (m)	Pixel Scale (mm)	Rover Heading (° from N)	Image Azimuth (° from N)	Date	L_s (deg)	Sol	LMST	LTST	Image ID	Compression	Abbreviation	Figures
					Sol 1204 Turn								
	15.06	1.11, 3.31	235.2	1.7	5/1/16	90.7	1214	12:50	13:06	MCAM05524	lossless	NwC4	
					Prebump to Gobabeb-Solitaire								
R0	2.82	0.21	345.6	342.4	8/1/16	92.1	1217	11:18	11:34	MCAM05583	85	GS1	14, S5
L0		0.62						16:00	16:16	MCAM05587	85	GS2	
L0_R0		0.21, 0.62			10/1/16	92.9	1219	12:15	12:31	MCAM05591	lossless	GS3	
R0		0.21						13:01	13:17	MCAM05588	lossless	GS4	
								15:00	15:16	MCAM05589	lossless	GS5	
								16:58	17:14	MCAM05590	lossless	GS6	
					11/1/16	93.4	1220	11:18	11:34	MCAM05593	lossless	GS7	
								13:39	13:55	MCAM05594	lossless	GS8	
								15:28	15:44	MCAM05595	lossless	GS9	
					Gobabeb-Hebron								
					Mastcam								
2 × 1 L0_R0	3.19	0.240, 0.70	340.0	25.2	13/1/16	94.3	1222	12:49	13:05	MCAM05606	lossless	GH(M)1	
1 × 2 R0		0.24		17.1	16/1/16	95.6	1225	13:55	14:12	MCAM05633	lossless	GH(M)3	
					17/1/16	96	1226	12:43	13:00	MCAM05637	lossless	GH(M)4	15a, S6a
								15:48	16:05	MCAM05638	lossless	GH(M)5	
					18/1/16	96.5	1227	12:31	12:48	MCAM05639	lossless	GH(M)6	
					19/1/16	96.9	1228	12:07	12:24	MCAM05648	lossless	GH(M)7	
					20/1/16	97.4	1229	12:18	12:35	MCAM05656	lossless	GH(M)8	
								15:56	16:13	MCAM05666	lossless	GH(M)9	
					25/1/16	99.6	1233	13:19	13:37	MCAM05702	lossless	GH(M)10	
					26/1/16	100.1	1235	14:00	14:18	MCAM05722	lossless	GH(M)11	
					27/1/16	100.5	1236	12:49	13:07	MCAM05729	lossless	GH(M)12	
								15:47	16:05	MCAM05730	lossless	GH(M)13	
					29/1/16	101.4	1237	14:02	14:20	MCAM05735	lossless	GH(M)14	
					30/1/16	101.9	1238	12:49	13:08	MCAM05742	lossless	GH(M)15	
								16:04	16:23	MCAM05743	lossless	GH(M)16	
					31/1/16	102.3	1239	13:03	13:22	MCAM05744	lossless	GH(M)17	
					1/2/16	102.8	1240	13:07	13:26	MCAM05753	lossless	GH(M)18	
								16:04	16:23	MCAM05756	lossless	GH(M)19	
					3/2/16	103.7	1242	15:59	16:18	MCAM05770	lossless	GH(M)20	
					RMI								
5 × 1	2.80	0.05	340.0	20.7	16/1/16	95.6	1225	14:09	14:26	CCAM01225	ICER 6, MINLOSS 2	GH(R)1	15b, S6b and S6c
					26/1/16	100.1	1235	14:31	14:39	CCAM03235	ICER 6, MINLOSS 2	GH(R)2	
					2/2/16	103.2	1242	16:12	16:31	CCAM02242	ICER 6, MINLOSS 2	GH(R)3	
					Dump Piles								
2 × 1 R0	2.31	0.17, 0.51	334.6	338.0	14/2/16	108.6	1253	12:21	12:42	MCAM05850	lossless	EF1	16, S7

[a]Column 1: Numbers refer to the number of frames in the mosaic. "R" and "L" are the Mastcam 100 mm and 34 mm cameras, respectively. Column 2: Target distances are from mast (Mastcam) or ChemCam (RMI) to the approximate center of the target field of view. Column 8: If in red, sol contains REMS blocks bridging intrasol imaging columns 9–10: Times at middle of sequence and rounded to nearest Martian minute. Columns 9–13: If in blue, only thumbnails downlinked.

Table 3a. REMS Blocks Associated With Change Detection Images During the Bagnold Dune Campaign, Ripple Crossing to in Front of Namib Dune[a]

	Local time hour							
Sol	10	11	12	13	14	15	16	17
1174					rc1			
1175								
1176					rc2			
1177				rc3				
1178					rc4			
1179								
1180								
1181								
1182								
1183								
1184								
1185								
1186								
1187								
1188								
1189								
1190								
1191								
1192								
1193								
1194								
1195								
1196								
1197					Nctx1			
1198			Nnf1, Ncs1, NIE1, NC1, NuC1					
1199		NuC2						
1200			Nnf2, NIE2, NC2, NuC3, Nctx2					
1201		Nctx3, NuC4, Nsf2	Nnf3, NIE3		NwC1			
1202	NuC5	Nnf4, NIE4, NC3, Nctx4, NwC2		Nnf5, NIE5, NC4, NuC6, Nctx5	NwC3			
1203					Nctx6, Nnf6, NIE6		Nnf7, NIE7	
1204					rd1		Ncs2	
1205								
1206		Nnf8, Ncs3, Nsfz8, rd2					Nnf9, Ncs4, NIE9	
1207								
1208								
1209								
1210		Nnf11, Ncs6, NIE11, rd3		Nnf12, Ncs7, NIE12	Nnf13, Ncs8, NIE13		Nnf14, Ncs9, NIE14	Nnf15, Ncs10, NIE15
1211				Nnf17				
1212								
1213								
1214			Ncs12, NIE17, NC5, Nctx7, NwC4					

[a]Labels refer to image IDs in Table 2 and the text. Times are local mean solar. The red color shows the timing of REMS extended blocks. The black text refers to the hour of the Martian sol at which a given change detection sequence took place. Details of these sequences are shown in Table 2.

Table 3b. REMS Blocks Associated With Change Detection Images During the Bagnold Dune Campaign, Solitaire to Dump Piles[a]

	Local time hour							
Sol	10	11	12	13	14	15	16	17
1215								
1216								
1217		GS1					GS2	
1218								
1219			GS3	GS4		GS5	GS6	
1220			GS7	GS8		GS9		
1221								
1222		GH(M)1						
1223								
1224								
1225				GH(M)2	GH(R)1			
1226			GH(M)3			GH(M)4		
1227			GH(M)5					
1228			GH(M)6					
1229			GH(M)7			GH(M)8		
1230								
1231								
1232								
1233				GH(M)9				
1234								
1235					GH(M)10, GH(R)2			
1236			GH(M)11			GH(M)12		
1237					GH(M)13			
1238			GH(M)14				GH(M)15	
1239				GH(M)16				
1240				GH(M)17			GH(M)18	
1241								
1242						GH(M)19	GH(R)3	
1243								
1244								
1245								
1246								
1247								
1248								
1249								
1250								
1251								
1252								
1253			EF1, EF2		EF3			

[a]Labels refer to image IDs in Table 2 and the text. Times are local mean solar. The red color shows the timing of REMS extended blocks. The black text refers to the hour of the Martian sol at which a given change detection sequence took place. Details of these sequences are shown in Table 2.

2.3.3. Drive Path

2.3.3.1. Ripple Crossing

Approaching High Dune (6 m tall), the rover parked from sols 1174 to 1178 near a ripple (the name "ripple crossing" refers to rover mobility tests over ripple crests conducted subsequently in this area). Mastcam mosaics were taken on sols 1174 and 1176–1178, including stereo on 1174 and 1176 (Table 2). REMS EBs were acquired between these images (Table 3a). However, the rover was not pointed in the optimum NNW direction, instead parked at 176.5° azimuth. Hence, the maximum daytime winds were likely not sampled.

2.3.3.2. In Front of Namib Dune

After an in situ investigation at High Dune in which no change detection experiments were performed, the rover drove in front of the lee face of Namib Dune (4 m tall) and parked at an azimuth of 235.5° (Figure 2).

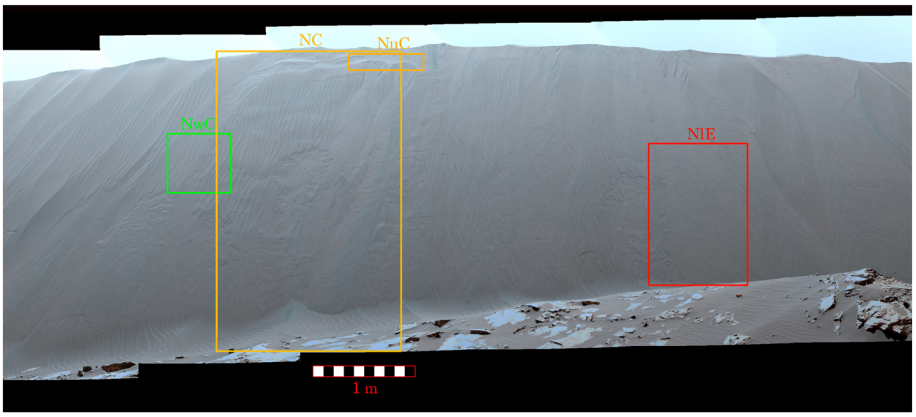

Figure 3. The slip face of Namib Dune as seen in a portion of Mastcam 34 mosaic MCAM05504 (sol 1201) at a distance of ~15 m. The boxes show locations of areas imaged for change detection: Namib west central (NwC), Namib central (NC; Figure 13 and Figures S4a and S4c), Namib upper central (NuC; imaged with RMI; Figure S4b), and Namib lower eastern (Nle). A scale bar appropriate for the center of the dune is shown below the mosaic. See Table 2 for image details.

The rover was in front of Namib Dune from sols 1198 to 1214, a period of 16 sols. On sol 1204 the plan had been to drive west out of the lee region and reorient the rover to a NNW orientation to best sample the strong regional winds and then remain parked there over the 2015–2016 holiday period (Table 2). However, a steering actuator fault caused by a voltage charge from a radioisotope thermoelectric generator short curtailed the activity such that no drive and only a 0.3° azimuth change was achieved. This occurred on 26 December 2015 within a 12 sol period of pre-planned autonomous activities during the holiday period such that recovery was not possible. In subsequent analysis, it was determined that this orientation was actually preferable given that the drive did not occur, because Namib Dune deflects the wind into a dominant westerly flow in front of the lee [*Newman et al.*, 2017]. During the time *Curiosity* was at this location, REMS EBs were acquired on all sols, with 11:00–12:00 records on each day except sols 1204 and 1206 (Table 3a).

Three classes of change detection observations were taken here. The first was imaging close to the ground, with the expectation that any sand movement would most easily be detected at the highest spatial resolution. Within this subcategory, two image sequences were used. The first was a continuation of the MSL clast survey, an ongoing campaign to image, using a single M34/M100 stereo pair, the ground at a fixed pointing geometry. Although intended for systematic sampling of the characteristics of clasts along the MSL traverse [*Yingst et al.*, 2016], the sequence was used here to look for wind-related changes while the rover was paused. Recognizing that a single location could be insufficient if any wind-related changes occurred elsewhere, an additional series of four near-field images was acquired eight times between sols 1198 and 1203. Later, this four-frame observation was augmented with five more near-field locations (for a total of nine) and acquired 10 times between sols 1206 and 1214. The near-field images (including the clast survey series) were acquired at 17 different times, including intrasol imaging on sols 1202 (twice), 1203 (twice), 1206 (twice), and 1210 (5 times), with four of the times on 1210 downlinked only as thumbnails. Clast survey images were acquired close in time to the near-field sequences on sols 1198, 1204, 1206 (twice), 1207, 1210 (5 times), 1211, and 1214. REMS EBs spanned the intrasol images on sols 1202, 1203, and 1210.

To reveal any broad changes affecting Namib Dune (closest point ~10 m away), such as avalanching or substantial ripple movement from high wind events, M34 mosaics of some or all of the lee face were acquired 7 times, including twice on sol 1202 during a REMS EB (Table 2). The 1202 and 1203 sequences were never returned at full resolution, as the mosaics from the other sols indicated no changes during this time.

The third class of change detection observations involved M100/M34 and RMI images and mosaics for three selected areas on Namib Dune (Figure 3). The dune lee face, the first one imaged closely on another planet, exhibits a suite of morphologies discussed and analyzed in detail by *Ewing et al.* [2017]. The main features are slope-parallel wind impact ripples on the lee face, grain flows (i.e., sand flows or grain avalanches) with characteristic theater-headed scarps and lobate toes, and, at the dune base, a basal sand apron mantled with large ripples and impact ripples. Fractures on the lee face are present and represent zones of detachment

of slightly cohesive sand. Ripples oriented parallel to the lee slope indicate modification by winds that have been deflected along the lee slope. A central area of the lee face was imaged with a 3 × 6 M34/M100 mosaic 5 times, including twice on sol 1202 with a spanning REMS EB. The 1202 and the 1214 mosaics were never returned at full resolution, as no changes were found between images taken in earlier and later sols. RMI also provided high-resolution imaging of the slump alcoves within and to the right of the upper western Mastcam field of view, with these mosaics varying from a single frame to 5 × 1 or 10 × 1 (Table 2). A REMS EB spanned the two 5 × 1 instances on sol 1202. Periodic 2 × 3 M34/M100 and 2 × 4 M100 mosaics were acquired of a lower, eastern area of the slip face (Figure 3) 18 times distributed over 10 sols, with multiple looks on four of these sols (with REMS EBs spanning the sol 1206 observations). The 1206, 1207, 1210, and 1211 instances were not returned at full resolution because other data indicated no changes during these times. Finally, single-frame stereo Mastcam images were acquired 4 times of transverse ripples and fractures within and mostly to the east of the central imaging area (Figure 3), with a REMS EB spanning the two instances on sol 1202. As in some other cases, other data indicated that these images would likely not show significant changes, so they were not returned at full resolution.

2.3.3.3. Solitaire

Curiosity next drove northwest toward Gobabeb at the western secondary slip face of Namib Dune. Prior to the final arrival at this location, M34 and M100 images of the target "Solitaire" were acquired on sol 1217 at two different times. This area consisted of rippled sand, rock outcrop, and cobble-sized float. Further imaging occurred on sols 1219 and 1220 (Table 2). REMS EBs spanned the intrasol imaging of this target on each sol.

2.3.3.4. Hebron

At Gobabeb, in situ studies were conducted that involved wheel trenching and the scooping of dune material, with two size fractions, <150 μm and 150–1000 μm, delivered to the Sample Analysis on Mars instrument [*Mahaffy et al.*, 2012], and the former also delivered to the CheMin instrument [*Achilles et al.*, 2017]. Other activities included Mastcam, Mars Hand Lens Imager (MAHLI) [*Edgett et al.*, 2012], Alpha-Particle X-ray Spectrometer [*O'Connell-Cooper et al.*, 2017], and ChemCam [*Cousin et al.*, 2017] investigations of the trench and grain-sorted dump piles, Mastcam photometry, active Dynamic Albedo of Neutrons (DAN) [*Mitrofanov et al.*, 2012] to assess subsurface hydrogen, and an investigation to determine the possible presence of nighttime-condensed frost on dune sand at this cold time of year. Change detection studies were focused on the target "Hebron," a slumped region on the lee face of a large ripple on the edge of the dune. With freshly exposed sand, this was chosen as an ideal area to monitor changes during the Gobabeb investigations. The initial Mastcam imaging was a 2 × 1 stereo mosaic on sol 1222, but the format was changed to a 1 × 2 R0 for sols 1225, 1226 (two intrasol observations), 1227, 1228, 1229 (2), 1233, 1235, 1236 (2), 1237, 1238 (2), 1239, 1240 (2), and 1242. The intrasol images on sols 1226, 1229, 1236, 1238, and 1240 were spanned by REMS EBs. RMI took 5 × 1 mosaics of Hebron on sols 1225, 1235, and 1242.

2.3.3.5. Dump Piles

After Gobabeb, *Curiosity* drove west until reaching High Dune, then northwestward along that dune's northeastern margin. Here the pre-sieve ("Dump F") and post-sieve ("Dump E") materials from the Gobabeb scoop #3 onboard analysis were dumped and examined. Subsequent MAHLI analysis found that the pre-sieved and post-sieved grain sizes actually ranged from ~100 to 500 μm and ~40 to 200 μm, respectively [*Ehlmann et al.*, 2017], hence there was some overlap in the range of grain sizes in both piles. Because of the short amount of time at this location, images were acquired only on sol 1253, at three different times bridged by a REMS EB.

2.4. Rover Image Analysis

Change detection Mastcam and RMI images of the same location were compiled, and if an image did not use the entire 8 bit potential dynamic range or if the range did not provide sufficient contrast in dark sand, it was stretched to bring out detail. Co-located images were overlaid in Adobe Photoshop as layers and then registered using the "auto-align layers" function. As can be seen in the supporting information, the resulting products provided a well-controlled set of images for which changes could be assessed. Given the nature of the changes found, which were mostly grain scrambling, our analysis is generally qualitative, noting the relative degree of changes between various intervals and on which sols these occurred.

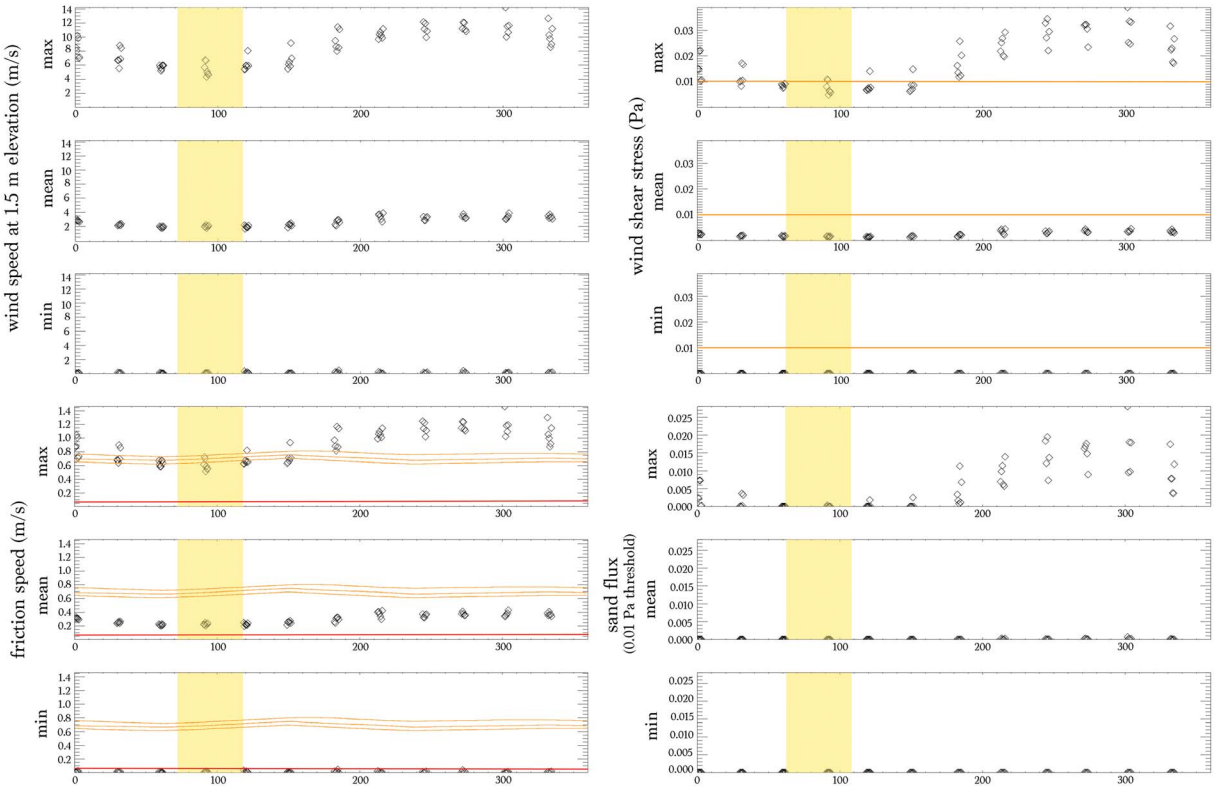

Figure 4. Seasonal variations in quantities relevant to sand motion, as predicted by the MarsWRF model for the grid point centered at 137.37°E, 4.69°S. Shown are the daily maximum, mean, and minimum values of: (top left) estimated wind speed at the 1.5 m height of the REMS wind sensor, (bottom left) friction speed ($u*$), (top right) shear stress τ, and (bottom right) relative sand flux assuming a 0.01 Pa threshold [*Ayoub et al.*, 2014], for 5 to 7 sols centered on each 30° increment of L_S. The 0.01 Pa threshold is shown as a horizontal orange line on the shear stress plots. Because $u* = (\tau/\rho)^{0.5}$, the 0.01 Pa threshold can be plotted as a function of friction speed as well, with the three curves corresponding to the minimum, mean, and maximum of atmospheric density (ρ) computed by MarsWRF. The solid red line corresponds to the minimum predicted impact threshold for basalt (Figure 1). Fluid thresholds exceed the upper y axis boundary thus are not shown. The yellow highlights in each plot show the seasonal range of the Bagnold Dune Campaign. This shows that the campaign occurred in a period of the year with low wind activity.

2.5. REMS Analysis

This paper does not include an extensive study of the REMS data set, on which other studies are focused [e.g., *Newman et al.*, 2017]. Rather, the intent is to use the wind results to provide some gauge of relative wind intensity over the times that the images were taken. We use the 5 min averages of the 1 Hz data set (see *Newman et al.* [2017] for more details of the averaging), which has been publicly released by the REMS team and is available in the Planetary Data System, but we also show 1 Hz REMS wind speed data for selected periods. For the latter, we focus on EBs covering the 11:00–12:00 and 14:00–16:00 local mean solar time (LMST) periods, intervals over which some of the highest winds occur in daytime measurements. In the case of the Solitaire site we also review the 12:00–14:00 time period that spans intrasol change detection images. We show the complete 5 min average wind magnitudes and directions over the entire campaign to get a broader sense of wind speed variation. The details of these derivations are described in *Newman et al.* [2017]. The 1 Hz wind data, which have not yet been publicly released, have been filtered by the REMS Team to remove erroneous measurements. Mean and median wind speeds for each 1 h EB, both with and without including individual wind measurements above the REMS team's current 20 m s^{-1} calibration confidence limit, are assessed. As will be shown, the relationship between REMS measurements and surface changes, with some notable exceptions, is not strong, indicating that rare gusts and other factors are likely driving grain movement in this season.

3. Results

3.1. MarsWRF

The MarsWRF results predict that the Bagnold Dune Campaign occurred during the lowest wind activity period of the year as shown by the seasonal variation of predicted 1.5 m wind speed, shear stress, friction speed,

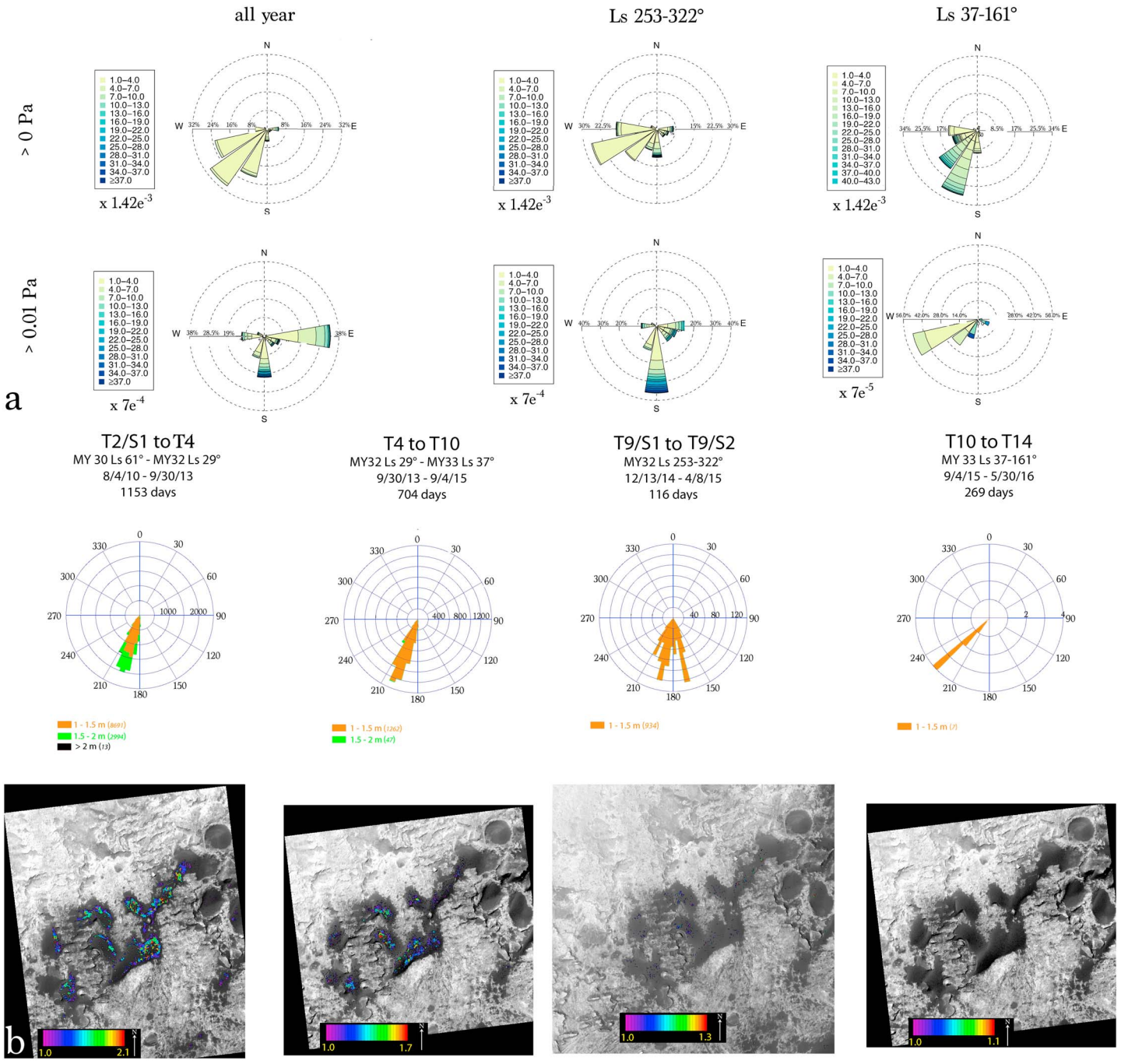

Figure 5. MarsWRF sand flux roses compared to HiRISE results. (a) Sand flux roses computed by MarsWRF. Here the roses are shown as the direction of the wind is blowing *toward* which is generally against convention but provides an easier comparison to the HiRISE displacement vectors. (b) At the top, HiRISE vectors computed from COSI-Corr-derived displacements on the dunes, shown as rose diagrams, subdivided by the amount of movement over the period indicated. At the bottom, the displacements are mapped onto the HiRISE image of the local dune field. The data on the left side of the figures correspond to a period of a Mars year (MarsWRF) or longer (the two HiRISE change detections at the left). The two sets of MarsWRF and HiRISE results at the right cover the same L_s intervals, with those second from right being L_s 253–322° and first from right being L_s 37–161°. The former corresponds to a higher flux season and the latter a lower flux season that overlaps with the time period of the Bagnold Dune Campaign. The roses from MarsWRF and the HiRISE results show good agreement and further show that the Bagnold Dune Campaign was conducted in a period of the year with little aeolian activity.

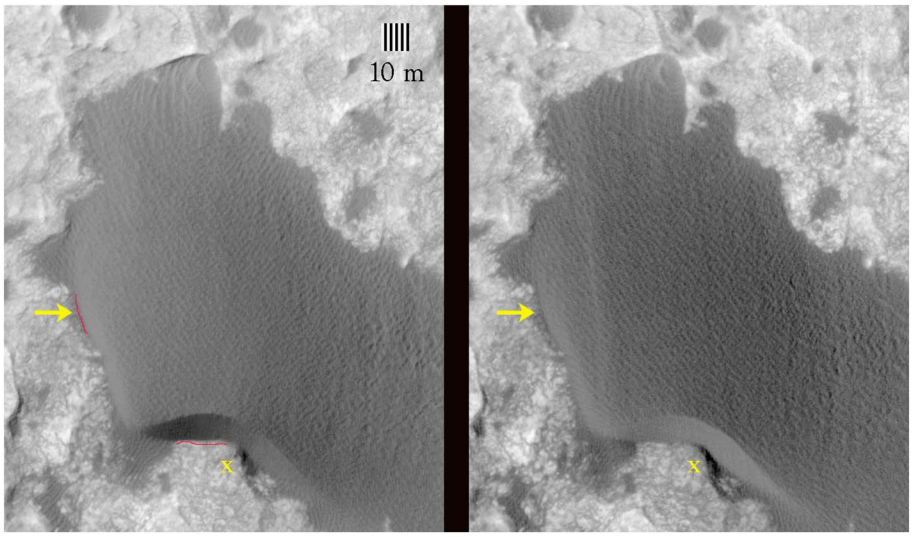

Figure 6. Namib Dune as seen in HiRISE images (left) PSP_009294_1750 (20 July 2008, Mars year 29, L_s = 101°) and (right) ESP_047416_1755 (7 September 2016, Mars year 33, L_s = 218°). The yellow *x* shows *Curiosity*'s location when it was parked in front of Namib Dune from sols 1196 to 1214. The yellow arrow shows the Gobabeb in situ site where the rover was located from sols 1216 to 1242. In the PSP_009294_1750 image (Figure 6, left), the red lines show the positions of the secondary and primary slip faces as seen in ESP_047416_1755. Over the 2971 Earth day period between the images, the primary slip face advanced as much as 1.75 m (7 HiRISE pixels), or ~0.2 m per Earth year. See Figure S1 for movies showing the changes between these and other images.

and potential sand flux (Figure 4). Superimposed on the shear stress plots, in orange, is the dune activity threshold of 0.01 Pa determined at Nili Patera [*Ayoub et al.*, 2014]. This is also shown on the friction speed plot, with the three sinusoidal curves representing values for the minimum, mean, and maximum atmospheric densities as they vary through the year. The red lines on these plots represent the minimum impact threshold for basalt on Mars as shown in Figure 1. The fluid threshold is not shown, as it exceeds the maximum value of the plots' *y* axis.

The predicted relative sand flux roses over three time periods are shown in Figure 5a. In this case, we break with normal convention in such plots and display the roses as the direction the sand is being transported *toward*, as opposed to coming *from*, in order to compare to the HiRISE change detection results, which we discuss below. The color and corresponding legends showing values up to 40 are relative dimensionless fluxes output by the model. Note the multiplicative factors under the scale bars; i.e., the lowest flux bin starts at $1.42e^{-3}$ in all three top row plots, at $7e^{-4}$ in the first two plots in the bottom row, and at $7e^{-5}$ in the third plot in the bottom row. The roses in the left column show predicted relative fluxes over an entire Mars year, with the top rose having a shear stress threshold of 0 Pa (i.e., no threshold) and the bottom 0.01 Pa. The former predicts significant sand transport to the southwest, whereas a higher threshold shows that considerable sand could be transported to the east. Restricting the L_s to the predicted high flux season (middle column) bounded by HiRISE image *T*9*S*1 and *T*9*S*2 (253°–322°) shows ESE transport for a 0 Pa threshold and dominantly southward direction for 0.01 Pa. Looking at the low flux period (right column) bounded by HiRISE images *T*10 and *T*14, and containing the time period in which the Bagnold Dune Campaign took place (Table 2), overall fluxes are significantly lower compared to the annual and peak time periods for the 0.01 Pa threshold condition (i.e., note the smaller multiplicative factor of $7e^{-5}$). Both threshold conditions show transport toward the southwest.

3.2. HiRISE-Derived Change Detection

The changes seen by HiRISE and quantified with COSI-Corr are shown in rose diagrams and maps in Figure 5b. A sense of overall activity is best seen by looking at the longest time interval, from images *T*2/*S*1 to *T*4 over a period of nearly two Mars years (1153 Earth days). Displacements are seen on all of the dunes but generally absent in sand trapped within small craters and other topographic lows, such as those in the eastern part of the maps. Comparing *T*2/*S*1–*T*4 over about two Mars years to *T*4–*T*10 over about 1 Mars year shows that the amount of displacement and the number of 2 m correlation pixels are proportional to time. Note that in the *T*2/*S*1–*T*4 case the elevation on the dune at which maximum displacements are measured is lower than for

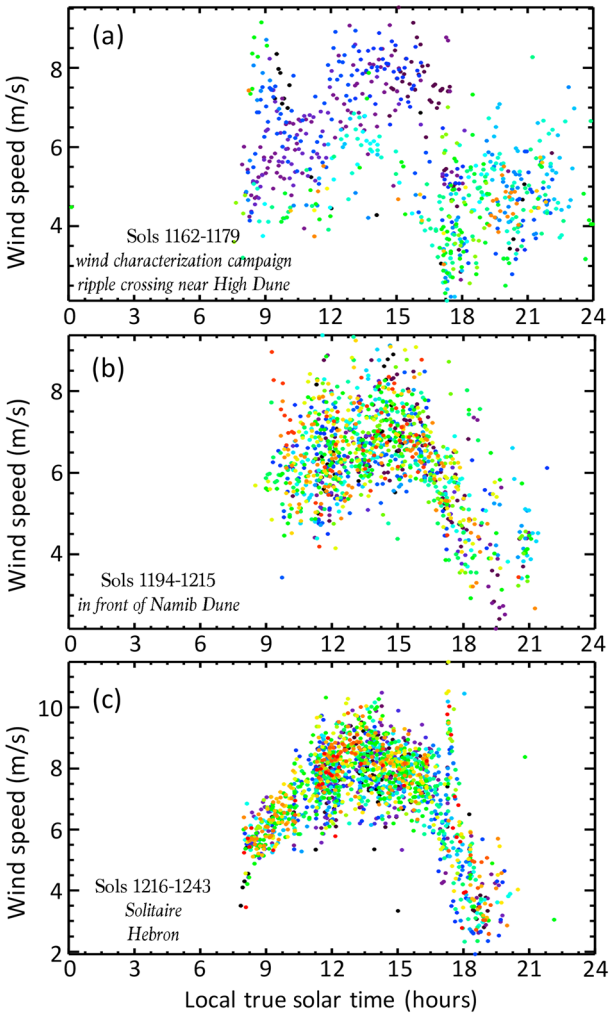

Figure 7. REMS 1 Hz wind speeds averaged over the first 5 min of each hour. The colors are coded relative to the sol range in reverse spectrum order, with purple representing the first sol and red the last sol in a given plot. (a) Sols 1162–1179 (starting with the wind characterization campaign prior to arriving at the Bagnold Dunes to the ripple crossing near High Dune. (b) Sols 1194–1215, corresponding to the time period in front of Namib Dune. (c) Sols 1216–1243, corresponding to the period of the rover approaching and parked at Gobabeb in which the change detection investigations of Solitaire and Hebron were conducted.

*T*4–*T*10. This is because above this elevation the ripples have moved so much that they cannot be tracked with the correlation software.

Looking at time scales shorter than a Mars year shows, not surprisingly, that displacements are less than over annual and longer baselines, with all values under 1.5 m. However, displacement is not proportional to the period between images but rather dependent upon season. In southern spring to summer (L_s = 253–322°), 934 2 m correlation pixels show displacement between 1 and 1.5 m, whereas only 7 are shown in fall to winter (L_s = 37–161°). The latter period contains the Bagnold Dune Campaign period of L_s = 73–109°.

In the annual and low flux time periods, the net displacement, as measured in the position of superposed ripples on the dunes' surface, is toward the SSW, whereas it is more southward in the high flux season. The direction of the HiRISE-derived roses shows close agreement with all of the Mars-WRF predictions except for the latter's simulation of annual fluxes using a threshold stress of 0.01 Pa predicting transport to the east. Other studies of dunes in Gale Crater over annual and longer time scales also consistently show transport to the south and west [*Silvestro et al.*, 2013, 2016], suggesting that the threshold of 0.01 Pa is biasing the MarsWRF results and that a lower threshold may be applicable to this part of Mars.

A visual assessment of changes can be seen by comparing the area of High and Namib dunes in images *T*1/*S*2 (in this case actually orthorectified to *T*2/*S*1 because of the lack of DEM coverage for the *T*1 pair) and *T*15. The primary and secondary slip faces clearly migrate, with the displacement of the former as great as 7 HiRISE pixels (1.75 m), which over this time interval corresponds to a displacement of ~0.2 m per Earth year (Figures 6 and S1a in the supporting information). The ripples on the surface of the dune have clearly moved a greater amount, as verified in the COSI-Corr results, and over this large time span cannot be confidently tracked. In looking at a movie using seven HiRISE images that span this time period (Figure S1b), changes over periods of a Mars year or more are obvious whereas those at shorter durations are much more difficult or impossible to recognize, especially in times of the year where sand fluxes are predicted to be low (~L_s 50–150° based on MarsWRF output; Figure 4).

3.3. MSL Bagnold Dune Campaign Change Detection Imaging and REMS Results

3.3.1. Overview

The diurnal variation in REMS wind speeds using averaged 1 Hz data from the first 5 min of each Martian hour shows that peak winds occur from ~11:30 to 18:00 in the vicinity of the dunes, and also at ~09:00 prior to

Table 4a. Mean and Median Values for REMS Blocks Associated With Change Detection Images, Ripple Crossing to in Front of Namib Dune (11:00–12:00, 14:00–16:00 LMST)[a]

	Rover Heading (deg)	Sol	Init Session	End. Session	Mean	Mean_below20	Median	Median_below20
Ripple crossing	176.5	1174	14	15	5.90	3.49	1.94	1.34
		1174	15	16	6.72	4.01	2.90	2.40
		1175	14	15	5.76	3.55	1.99	1.58
		1175	15	16	6.04	3.64	2.24	1.85
		1176	11	12	5.93	3.73	2.19	1.76
		1177	11	12	4.99	3.30	1.84	1.60
		1178	11	12	5.90	3.69	2.10	1.69
In front of Namib Dune	235.5	1194	14	15	6.83	5.09	4.27	4.06
		1194	15	16	6.60	4.72	3.87	3.67
		1198	11	12	6.30	4.65	3.82	3.51
		1198	14	15	6.99	5.12	4.16	3.82
		1198	15	16	7.30	5.75	4.83	4.54
		1199	11	12	6.15	4.99	4.05	3.82
		1200	11	12	6.00	4.67	3.74	3.50
		1201	11	12	6.03	4.87	3.86	3.67
		1202	11	12	6.58	5.07	4.26	4.03
		1202	14	15	6.39	4.62	3.57	3.32
		1202	15	16	7.03	5.51	4.46	4.24
		1203	11	12	6.21	4.74	3.84	3.61
		1203	14	15	6.91	4.87	3.76	3.39
		1203	15	16	6.63	5.14	3.83	3.64
		1204	11	12	4.80	3.47	2.31	2.12
	235.2	1205	11	12	7.29	5.94	5.14	4.90
		1206	11	12	6.87	5.58	4.50	4.07
		1206	14	15	6.97	5.12	4.15	3.83
		1206	15	16	6.99	5.11	3.92	3.67
		1207	11	12	6.20	4.88	3.85	3.55
		1208	11	12	6.67	5.42	4.53	4.30
		1208	14	15	7.31	5.33	4.30	4.05
		1208	15	16	6.89	5.09	3.87	3.65
		1209	11	12	6.75	5.27	4.35	4.10
		1209	14	15	7.10	5.12	4.19	3.86
		1209	15	16	6.89	5.25	4.11	3.88
		1210	11	12	6.38	5.02	4.02	3.78
		1210	14	15	6.90	4.90	3.91	3.61
		1210	15	16	7.06	5.67	4.56	4.36
		1211	11	12	6.82	5.53	4.74	4.45
		1211	14	15	6.11	3.74	2.38	2.15
		1211	15	16	7.38	5.76	4.65	4.43
		1212	11	12	6.75	5.40	4.50	4.26
		1212	14	15	7.32	5.77	4.79	4.56
		1213	11	12	6.25	4.80	3.87	3.61
		1213	15	16	6.87	5.12	3.97	3.81
		1214	11	12	5.81	4.25	3.37	3.07

[a]The filled colors are spectrum-correlated to relative values within each column and change detection site.

Table 4b. Mean and Median Values for REMS Blocks Associated With Change Detection Images, Solitaire to Dump Piles (11:00–12:00, 14:00–16:00 LMST[a])[b]

	Rover Heading (deg)	Sol	Init Session	End. Session	Mean	Mean_below20	Median	Median_below20
Solitaire	345.6	1217	11	12	7.24	5.86	4.96	4.72
		1217	14	15	7.89	5.71	4.87	4.65
		1217	15	16	7.96	5.73	4.73	4.54
		1219	14	15	8.00	5.99	5.05	4.81
		1219	15	16	8.06	6.14	5.11	4.86
		1220	11	12	7.08	5.47	4.78	4.54
		1220	12	13	8.64	6.82	6.11	5.78
		1220	13	14	8.38	6.19	5.52	5.22
		1220	14	15	7.60	5.44	4.87	4.59
		1220	15	16	8.16	5.86	4.90	4.63
Hebron	340.0	1222	11	12	8.33	6.49	5.63	5.27
		1223	11	12	7.58	5.70	4.87	4.61
		1224	11	12	7.72	6.42	5.54	5.34
		1225	11	12	7.83	5.94	5.28	5.01
		1226	11	12	7.87	6.07	5.30	5.04
		1226	14	15	7.77	5.44	4.73	4.45
		1226	15	16	7.86	5.48	4.52	4.31
		1227	11	12	8.02	6.20	5.29	4.98
		1227	14	15	7.84	5.68	4.82	4.57
		1227	15	16	7.81	5.28	4.55	4.43
		1228	11	12	7.66	5.93	5.20	4.94
		1229	14	15	7.67	5.42	4.72	4.50
		1229	15	16	7.70	5.22	4.44	4.23
		1230	11	12	7.56	5.71	4.98	4.76
		1230	14	15	7.19	4.60	3.72	3.49
		1230	15	16	7.51	5.12	4.29	4.18
		1231	11	12	7.83	6.29	5.48	5.18
		1231	14	15	7.97	5.54	4.79	4.51
		1231	15	16	8.53	5.50	4.74	4.51
		1232	11	12	7.72	5.76	5.04	4.78
		1232	14	15	8.00	5.47	4.74	4.49
		1232	15	16	7.63	5.29	4.41	4.20
		1233	11	12	7.71	5.92	5.20	4.96
		1233	14	15	8.22	5.84	5.17	4.91
		1233	15	16	7.50	5.21	4.41	4.22
		1234	14	15	7.50	5.38	4.70	4.49
		1234	15	16	7.59	5.14	4.29	4.14
		1235	11	12	7.81	5.75	5.13	4.84
		1236	11	12	8.31	6.53	5.60	5.25
		1236	14	15	8.11	5.77	5.07	4.80
		1236	15	16	7.62	5.11	4.31	4.10
		1237	11	12	7.59	5.69	5.16	4.89
		1238	14	15	7.91	5.63	4.94	4.70
		1238	15	16	7.81	5.42	4.54	4.36
		1239	14	15	8.11	5.64	4.91	4.63
		1239	15	16	9.14	5.98	5.13	4.58
		1239	11	12	8.13	6.30	5.60	5.38
		1240	11	12	8.22	6.37	5.50	5.28
		1241	11	12	8.05	6.16	5.56	5.26
		1242	11	12	7.85	6.05	5.25	5.02

Table 4b. (continued)

	Rover Heading (deg)	Sol	Init Session	End. Session	Mean	Mean_below20	Median	Median_below20
Dump Piles	334.6	1253	12	13	8.74	6.76	6.16	5.86
		1253	14	15	8.43	5.71	4.89	4.65
		1253	15	16	7.25	5.87	5.00	4.81

[a]12:00–14:00 and 12:00–13:00 also shown on sols 1220 and 1353, respectively; see text for details.
[b]The filled colors are spectrum-correlated to relative values within each column and change detection site; the red text for Solitaire, and Dump Piles show when changes seen in the images occurred.

reaching Namib Dune (Figure 7). The five areas studied for change detection with *Curiosity* (ripple crossing near High Dune, Namib Dune lee region, Solitaire, Hebron, and the dump piles) were extensively imaged, as well as sampled with REMS EBs (Tables 2–4). The variations among the measured winds at these sites are seen by comparing the mean and medians for all 11:00–12:00, 14:00–15:00, and 15:00–16:00 extended blocks obtained at each location (Tables 4a and 4b and Figures 8 and 9). These EBs were chosen for having some of the maximum wind speeds for periods that could be measured, i.e., periods outside of the coldest times of sol when the wind data were too noisy and wind speeds are unknown [*Newman et al.*, 2017]. Although these results show an approximate increase in typical wind speeds with sol, the results are biased by the rover orientation and location. In the case of the ripple crossing site, the rover was facing nearly due south (azimuth 176.5°) and therefore facing the wrong way to best sample the strongly northwesterly winds that dominate daytime measurements in this area [*Newman et al.*, 2017]. As discussed above, at Namib Dune *Curiosity* was pointed WSW, but in this case, because of flow around the dune resulting in strong westerly circulation, this orientation was optimal. The Solitaire, Hebron, and dump pile change detection observations were all achieved with the rover at the optimum northwesterly heading. The mean and median results illustrate general trends but do not show the peak winds that are likely the strongest drivers for surface change. A sense of dominant *measured* wind directions and azimuths, and how these are influenced by rover heading, is shown in Figure 9 where relative 5 min average winds are plotted to show azimuth and magnitude. Periods with large numbers of red arrows (indicating that rear winds dominate) are unlikely to provide representative speeds, because very few retrievals during those periods were from the primary wind direction.

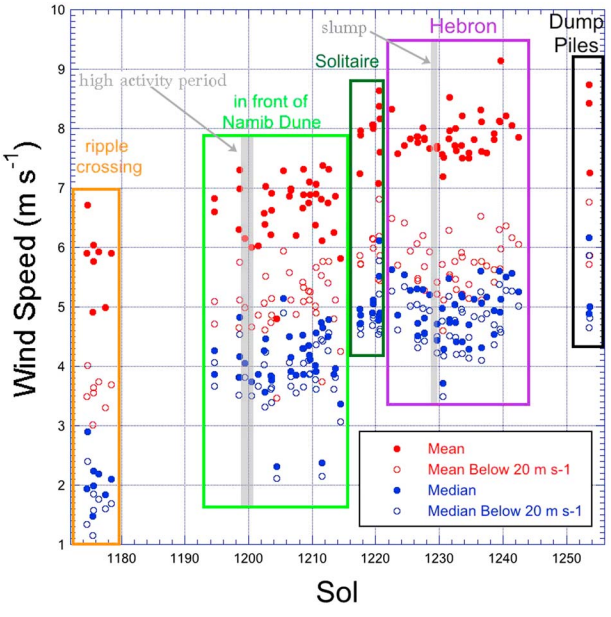

Figure 8. REMS-derived 1 Hz wind speeds measured in the Bagnold Dune campaign at each change detection site. These means and medians are computed over 1 h blocks from 11:00–12:00, 14:00–15:00, and 15:00–16:00 (12:00–14:00 and 12:00–13:00 are also shown for sols 1220 and 1353, respectively). Two events of high surface activity are shown in gray. Also see Tables 4a and 4b.

As we show below, only at the Solitaire and dump pile sites could intrasol changes be documented, as particle displacements or appearances/disappearances were significant enough to see. At other locations, where any changes are more subtle, varying illumination conditions challenged the identification of any moving grains that constitute the majority of observed activity. At the outset when these sequences were designed it was recognized that only major changes at the scale of displaced ripples or significant movement of grain patches would be seen in images separated by a few hours at different illumination conditions. Therefore, the following discussion largely consists of intersol changes, for which timing can in some cases be constrained to a single sol interval. Where available, we compare changes to the <20 m s^{-1}

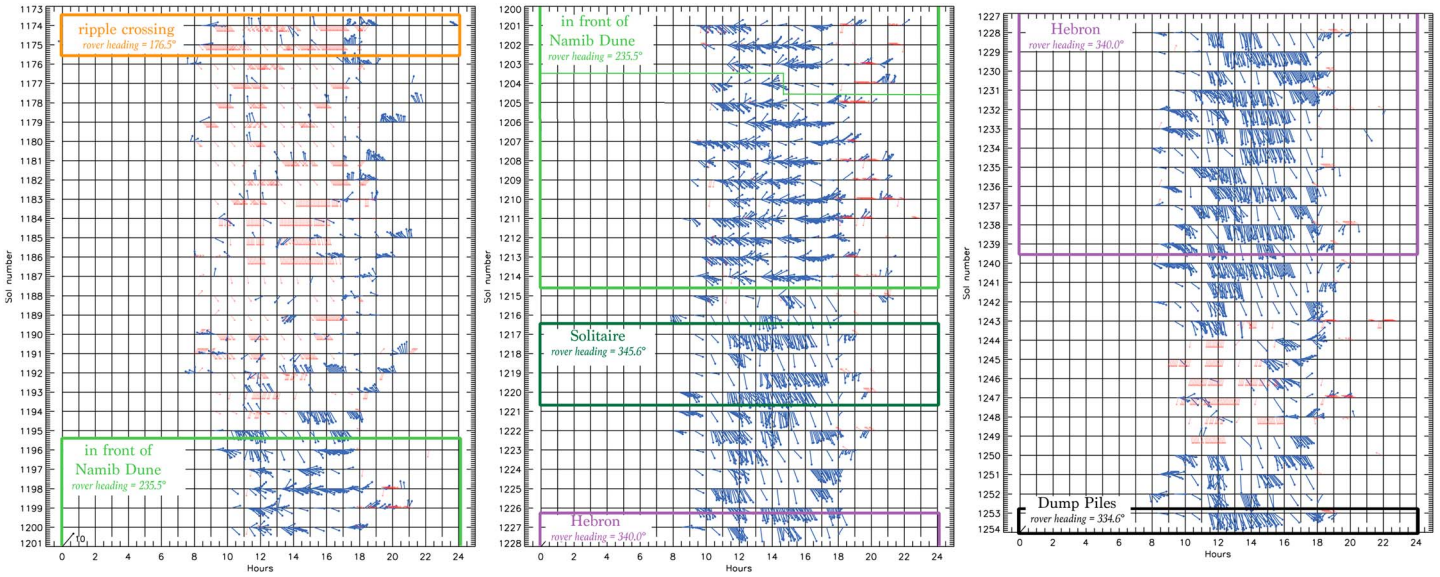

Figure 9. REMS wind retrievals. The arrows point in the 5 min-average wind direction for front winds, and their length is proportional to the average wind speed, scaled by the black arrow at the bottom left of the plot. The arrows pointing up the page indicate winds blowing toward the north (wind direction 0°), whereas the arrows pointing toward the right indicate winds blowing toward the east (wind direction 90°). The red arrows are times with primarily rear winds, with the arrow pointing to the middle of the quadrant into which the wind blew. Hence, the red arrows have only two possible orientations over any period with a constant rover heading. No wind speeds are retrieved for rear winds; hence, all the red arrow lengths are equal and do not indicate speed. See the text and *Newman et al.* [2017] for further details.

REMS 1 Hz wind speed histograms from 11:00–12:00, 14:00–15:00, and 15:00–16:00. A summary of the means and medians for these hour time periods where they are within imaging sequences is shown in Figure 8. All REMS retrievals during the Bagnold Dune Campaign, including the 5 min hour results, are summarized in Figure 9. These hour blocks associated with the ripple crossing, Namib, Solitaire, and the dump pile change detection sequences are shown in Figures 10, 11, 14, and 16, respectively. In our discussion, we commonly refer to images or mosaics with an abbreviation associated with their location (e.g., "rc" for ripple crossing) and a following number indicating the relative timing within that particular change detection campaign (e.g., "rc4" for the fourth ripple crossing image). The times and other ancillary data associated with these images are tabulated in Table 2 and how they map to REMS blocks (in LMST hours) is shown in Tables 3a and 3b.

3.3.2. Ripple Crossing Near High Dune

Over the 3 sols (1174, 1176, and 1178) of imaging between ~14:00 and 15:00 LTST, changes are seen between both sol gaps in the form of a small number of larger, more resolvable grains either "disappearing" or being slightly displaced (Figures S2a–S2c). Activity is particularly apparent on the right (~west) side of the ripple (Figure S2c). The maximum size of moving grains subtends only around 2 pixels in the M100 images, or ~400–500 μm, and most are somewhat brighter than the more abundant, finer sand. On the soil near the foreground rocks (Figures S1a and S1b), many of the changing grains seem to "disappear" from one frame to the next indicating that they either moved out of the field of view or were displaced too far to be recognized in their new positions. On the ripple (Figure S2c) many more moving grains are traceable from one frame to the next. Those grains that can be tracked generally move from lower left to upper right which, based on the Mastcam pointing azimuth of 191° (Table 1), is westward. Displacements, where recognized, are 4 mm or less but, given that some grains cannot be tracked, many grains, including small ones not resolved, likely moved farther. The degree of activity is greater between sols 1174 and 1176 than between 1176 and 1178. This seems to show a good qualitative agreement with mean and median wind speeds in the 11:00–12:00,14:00–16:00 blocks, with the highest values on sol 1174, 15:00–16:00, and the lowest on sol 1177, 11:00–12:00 (Table 4a and Figure 10).

3.3.3. In Front of Namib Dune

Over the sol range when *Curiosity* was in front of Namib Dune, multiple REMS EBs were acquired. Mean wind speeds in the 11:00–12:00/14:00–16:00 EB periods vary from ~4 to 7 m s^{-1}, have modes between 0 and 5 m s^{-1}, and are strongest from the west (Table 4a and Figures 9 and 11). These records provide

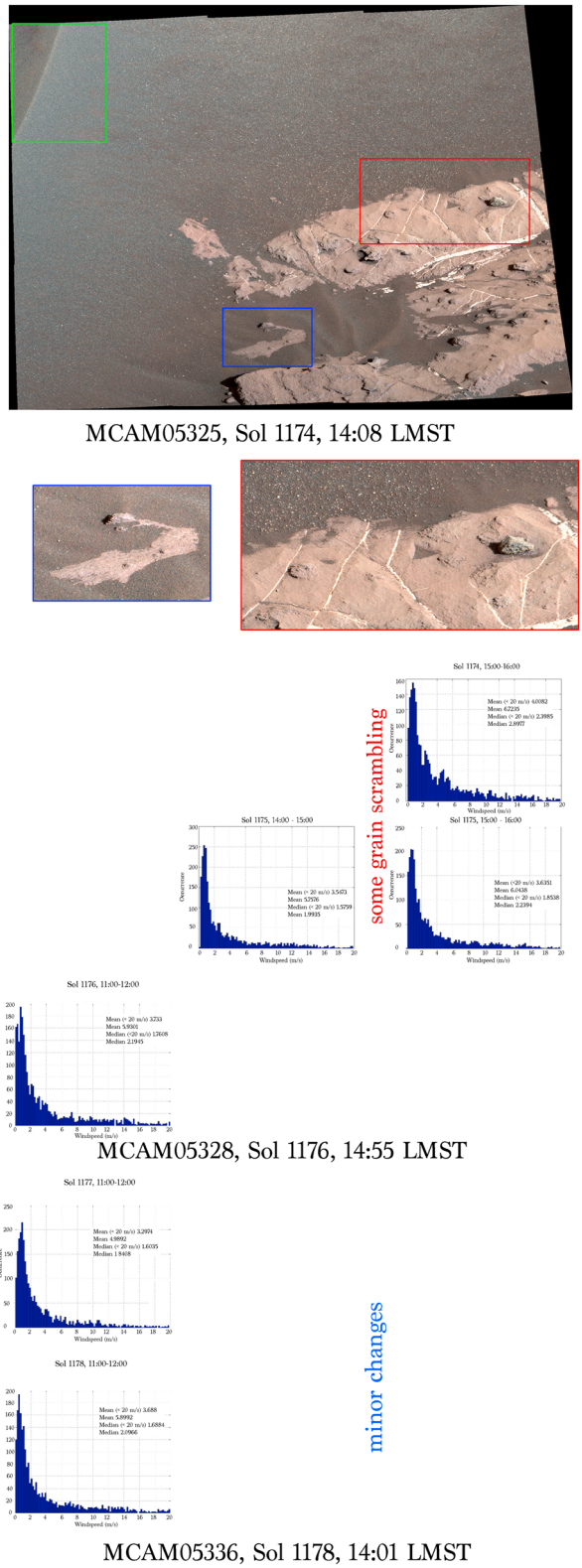

Figure 10. The ripple crossing change detection site near High Dune (see Figure 2) and associated REMS extended blocks. The top image shows the study area with the boxes showing the locations of the enlargements below and in Figures S2a–S2c. REMS 14:00 to 16:00 EBs were only available in the period during which changes took place.

important information on wind flow around the dune independent of the interest in change detection [*Newman et al.*, 2017].

Close to the rover, the distributed Namib near-field (Nnf) M100 sequence and clast survey (Ncs) sequence provide images with ground resolution near 0.2 mm/pixel (Figure 12). Not including thumbnails and compressed images, and restricting comparisons to midday images (11:21–12:42 LMST; 11:34–12:56 LTST), data were obtained on sols 1198 (Nnf1, Ncs1), 1200 (Nnf2), 1201 (Nnf3), 1202 (Nnf4), 1206 (Nnf8, Ncs4), 1210 (Nnf11, Ncs7), and 1214 (Nnf17, Ncs13). In the near-field observations, and focusing on the four images acquired at every instance (including when the larger nine frame version was run), some surface activity occurs between all sols, but is most apparent between sols 1198 and 1200, with scrambling of grains on the stoss side of some ripples and in the rover-disturbed areas of frame 3 (Figures S3a–S3d) (here "scrambling" refers to grain movements without a uniform direction of displacement.) The clast survey images show grain scrambling on the rippled sand and bedrock between sols 1206 and 1210, but little change from sols 1198 to 1206 and 1210 to 1214 (Figure S3d).

The center of the dune lee face was about 15 m from *Curiosity*, or about 6 times farther than the distributed near-field and clast survey images (Figure 3). In examining the M100 and RMI images of the lee face, changes were found in three locations (Figure 13). Between sols 1198 and 1200, on the western edge of the western alcove near the top of the lee face, a small secondary alcove eroded headward a distance slightly greater than 1 cm (based on a change of 11 pixels and an M100 scale of 1.1 mm/pixel at this distance) and formed a small ($<$ 1 cm wide) grain flow deposit (Figure S4a). Another grain flow of about the same size formed on the eastern edge of the alcove during the same interval. Across the lee in this area various bright pixels changed position,

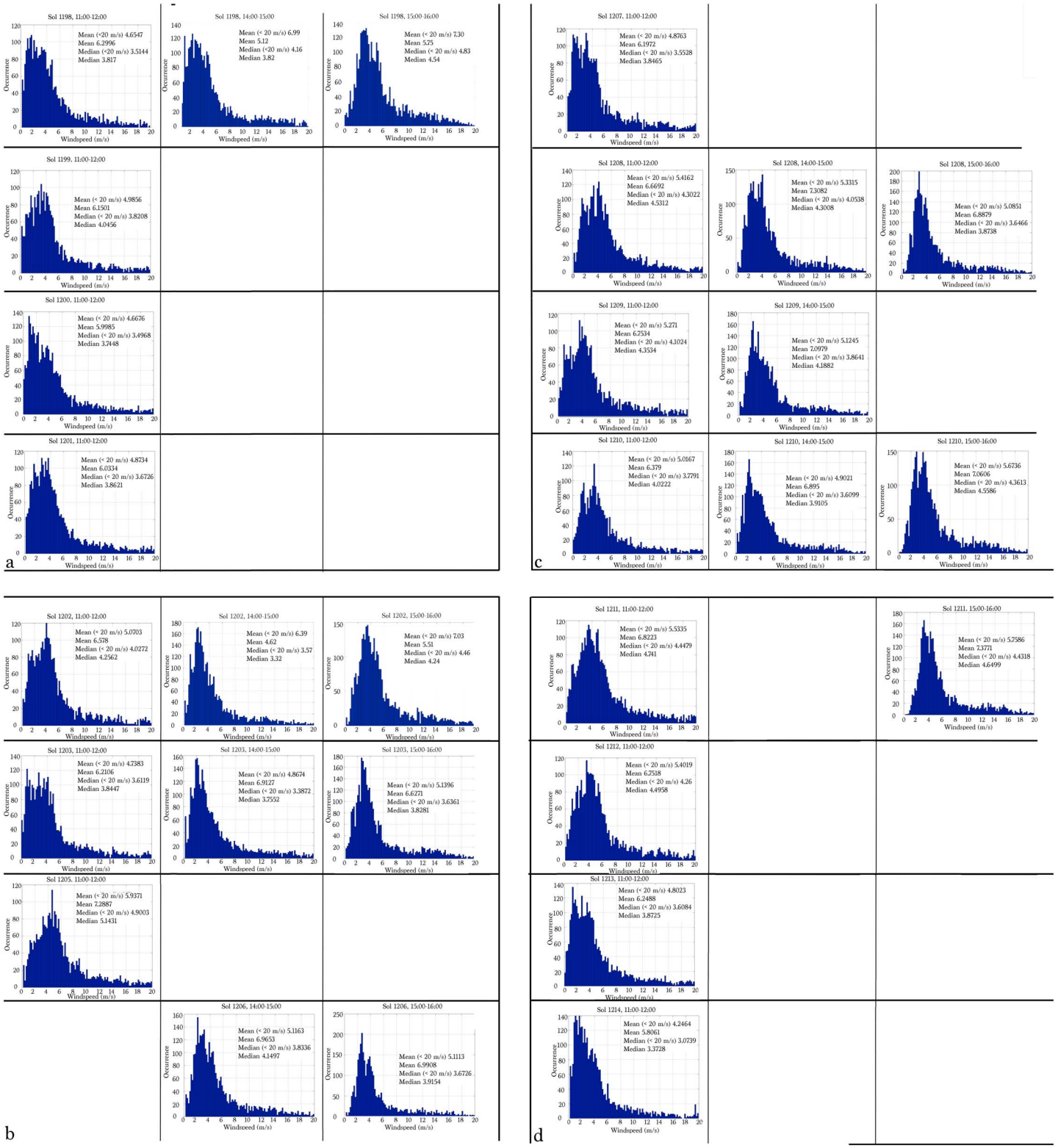

Figure 11. All of the 11:00–12:00 and 14:00–16:00 filtered 1 Hz results from REMS extended blocks that occurred while *Curiosity* was in front of Namib Dune. (a) Sols 1198–1200; (b) sols 1202, 1203, 1205, and 1206; (c) sols 1207–1210; and (d) sols 1211–1214.

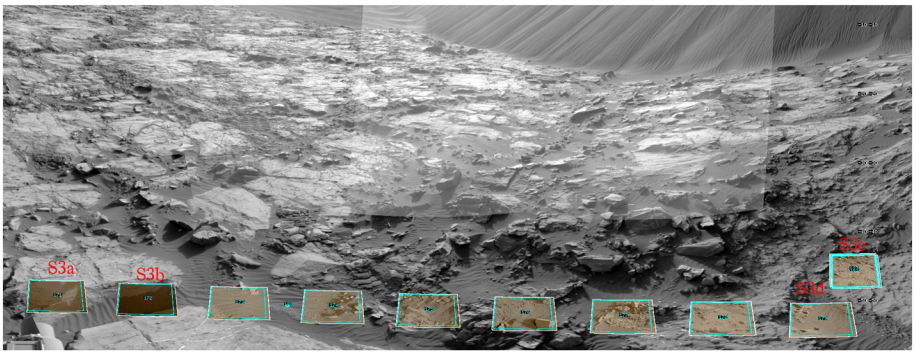

Figure 12. The location of the (bottom) nine near-field and (upper right) one clast survey change detection frames as shown overlaid on a Navcam mosaic. This is a portion of the of the "finder mosaic" product produced by the MSL Team. The red text indicates the location and name of the supporting information.

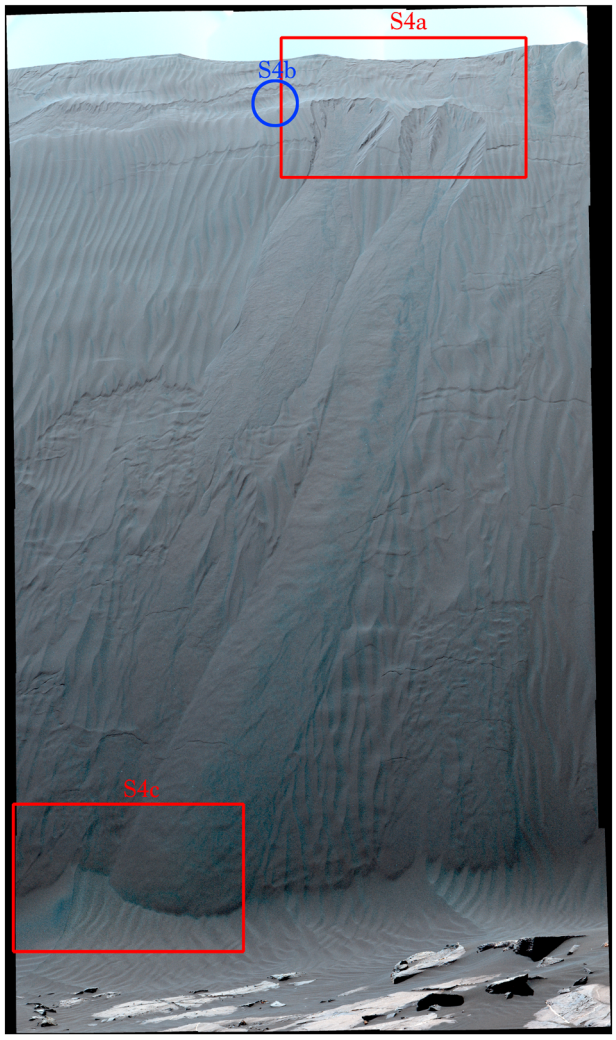

Figure 13. The Namib central imaging location seen in Mastcam R0 mosaic MCAM05491 acquired on sol 1198 (see Figure 3 for context). The distance to the slip face is about 15 m. The red and blue outlines show the field of view of the supporting information for Mastcam and RMI, respectively.

but in M100 images it is ambiguous whether these represent moving grains or specular reflections from sand grain microfacets. However, in RMI images, possible grain movement from right to left (so from the east to the west) can be seen in the western-most imaged region on the transverse ripple sets on the lee face. This location was imaged only twice, as part of the leftmost frame of the two 10 × 1 RMI mosaics obtained on sols 1200 and 1201 (the RMI mosaics are anchored to their rightmost frame; hence, the 5 × 1 mosaic does not overlap with frames 6–10 in the 10 × 1) (Figure S4b). The possible grains are about 3–4 pixels across which at this range corresponds to diameters of about 1 mm. The migration direction perpendicular to ripple crests is consistent with winds shaping bedforms on the lee side of the dune. Finally, at the bottom of the slip face, between sols 1198 and 1200, there is evidence for grain scrambling, for some of which east-to-west trends can be inferred (Figure S4c).

Results from the near-field (including clast survey) sequences, the formation of the secondary grain flows, and grain scrambling at the lee base of the lee slope, all suggest that some wind-related surface activity occurred between sols 1198 and 1200. The near-field/clast data are most definitive, as they had the highest spatial resolution and temporal sampling. In terms of the chosen REMS EBs, sol 1198 has coverage from

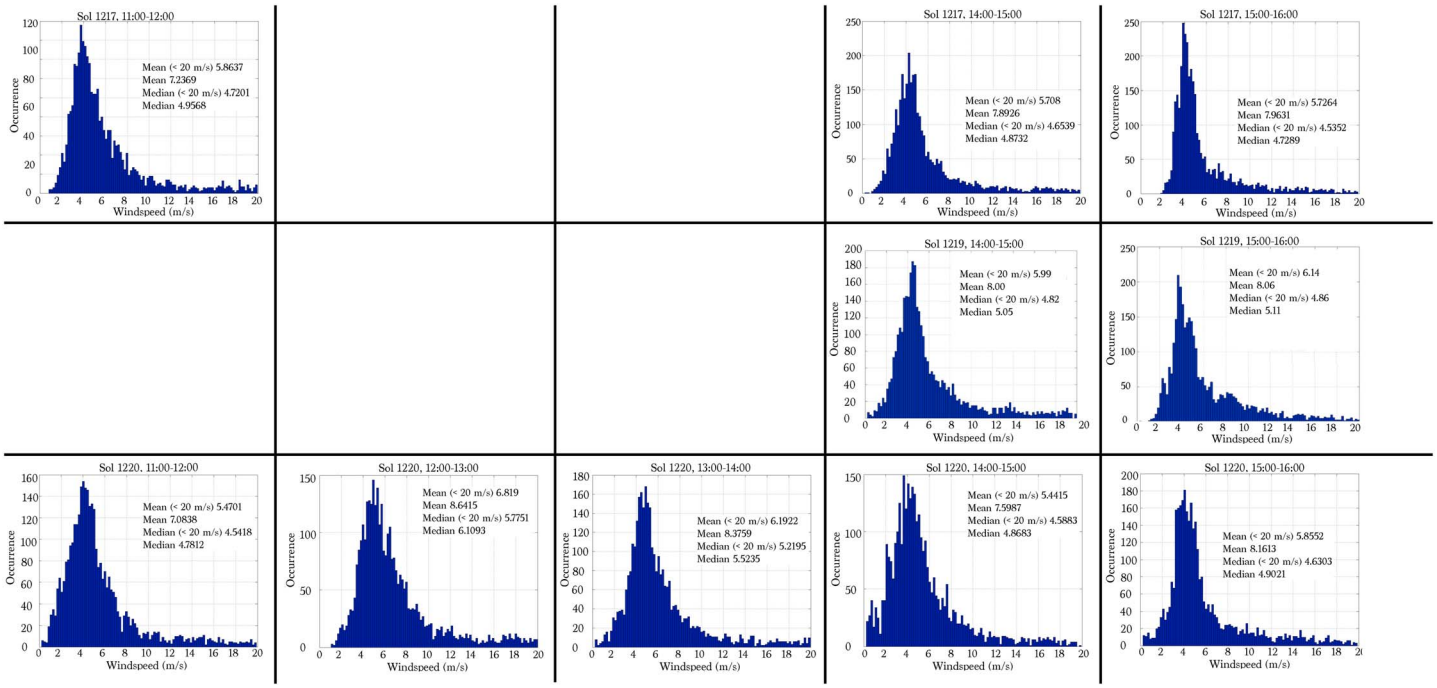

Figure 14. All of the 11:00–16:00 REMS filtered 1 Hz results that occurred while *Curiosity* was at Solitaire.

14:00–16:00, while sols 1199 and 1200 have coverage from 11:00–12:00. Both periods are amply covered in other sols (see Figure 9), thus it is noteworthy that the 15:00–16:00 period on sol 1198 had the second highest median wind out of all 11:00–12:00 and 14:00–16:00 Namib EBs, the third highest median wind speed if restricted to $<$20 m s^{-1}, and the fourth highest mean speed using both criteria (Table 4a and Figure 7).

3.3.4. Solitaire

The Solitaire near-field M100 observations show a limited amount of grain scrambling over 3 sols (Figure S5). From sol 1217/11:34 LTST (GS1) to 1219/13:17 (GS4) to 1220/11:34 (GS7) several 2–3 pixel (~0.5 mm) bright grains appear or disappear, with no confidence of movement direction over this duration. Because image GS6 on sol 1219 had very low Sun illumination (17:14 LTST), it could not be used to refine the timing of the changes between GS4 and GS7. However, solar illumination was similar enough to see intrasol changes between GS7 and 1220/15:44 (GS9) (GS8 was returned only in thumbnail format), including the appearance of one bright grain about 4 pixels (~0.8 mm) in size. It is noteworthy that the highest mean and median value recorded in the selected EBs, over the entire Solitaire observation period, occurred in sol 1220/13:00–14:00, i.e., between the GS7 and GS9 images (Table 4b). And if all 11:00–16:00 EBs during this period are considered, the highest mean and median values were in Sol 1220/12:00–13:00 (first line of red text in Table 4b; Figure 14), also between the two images.

3.3.5. Hebron

The target Hebron, at the Gobabeb site on the western margin of Namib Dune, was ideal for change detection observations (Figure 15a). A slump deposit close to the rover offered the chance to study potential wind effects on a metastable slope of loose Martian sand. Unlike the other sites investigated, the sands in the Gobabeb region are well characterized from in situ studies [*Ehlmann et al.*, 2017]. Grain size varies from 50 to 500 μm. The grains are composed of an ~65% crystalline material and 35% of an amorphous phase; plagioclase, pyroxene, and olivine make up about equal proportions of the crystalline fraction [*Ehlmann et al.*, 2017]. As seen in the 0.24 mm/pixel M100 mosaic of Figure 15, the sand can be subdivided into a background, unresolved ruddy brown fraction, and larger, more easily resolved grains that are either brighter or darker. These larger grains were subject to scrambling (i.e., displacements with no uniform direction of motion) in midday change-monitoring images. Movements were observed between sols 1227 and 1228, and between sols 1238 and 1239 (Figure S6a). A detachment scar starts to enlarge, with about 2 pixels (0.5 mm) of displacement, between sols 1226 and 1227, then 2–3 pixels (0.5–0.7 mm) more between sols 1227 and 1228, followed by a break and slump of about 9 mm between sols 1228 and 1229. Further slump motion of

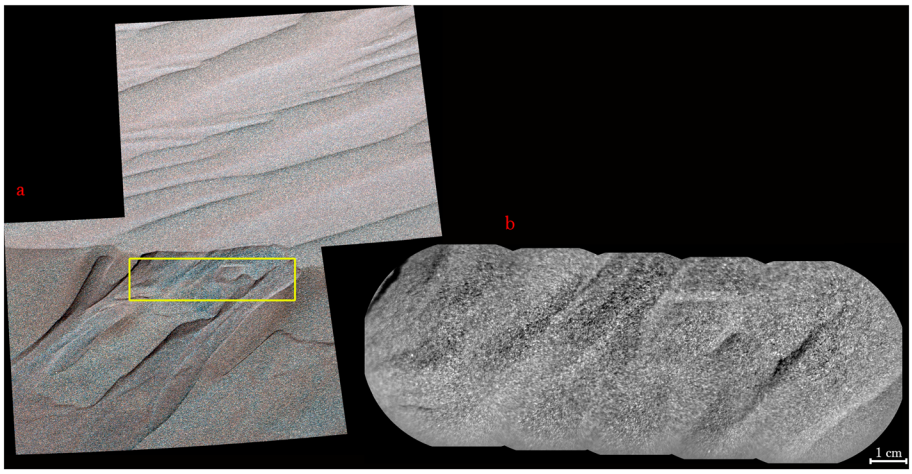

Figure 15. The Hebron change detection site. The location is on the lee of a large ripple that likely slumped because of rover activity. (a) Mastcam R0 mosaic MCAM05637 taken on sol 1226 from a distance of 3.2 m. The yellow box shows the approximate field of view of the RMI mosaic shown in Figure 15b. (b) RMI mosaic CCAM01225 taken on sol 1225 from a distance if 2.8 m. At this range, the pixel scale of RMI is ~50 μm.

1–2 mm occurred between sols 1229 and 1236, followed by very minor pixel level changes at the detachment scar between sols 1239 and 1240. RMI images show significant details of grain scrambling and headward erosion of the new slump deposit (Figures 15b and S6b and S6c). The REMS record does not seem correlated to any events at Hebron, although there are no 14:00–16:00 REMS EBs for sol 1228 that otherwise might have shown some high wind activity. Therefore, although the slump deposit could have been wind induced, other triggering mechanisms are possible.

3.3.6. Dump Piles

After onboard analysis was completed of the pre-sieved and post-sieved dump piles from scoop #3 at Gobabeb, these materials were discarded on the ground further along the rover's traverse near High Dune (Figure 2) and provided the opportunity for intrasol (sol 1253) change detection of loose, unconsolidated sand. As discussed above, the actual grain size ranges were determined to be ~100–500 μm and ~40–200 μm, respectively [*Ehlmann et al.*, 2017]. As with other intrasol change detection analyses, lighting geometry inevitably changed between the first and last images acquired at 12:42 and 15:06 LTST, respectively (Table 2). Nevertheless, over this time span of slightly more than 2 h, changes occurred to both piles (Figure S7). The M100 ground resolution is about 0.17 mm/pixel, allowing changes involving larger grains to be more easily recognized. In the post-sieve pile, several ~500 μm bright particles appear or disappear between the frames. Similar particles seem absent from the pre-sieve pile. However, over the 2 h time period, the left margin of the main pre-sieve pile, where it contacts the bright bedrock vein, moved ~1–2 pixels (0.2 mm) to the left, which is ~ESE based on the instrument pointing azimuth. The hourly summaries of the REMS EBs spanning 12:00 to 15:00 on sol 1253 show that mean wind speeds are higher than for all but two Hebron data points, and the mode of the wind speed of 5.8–6.0 m s^{-1} from 12:00 to 13:00 (second row of red text in Table 4b) is greater than the other blocks analyzed during the campaign (Figure 16).

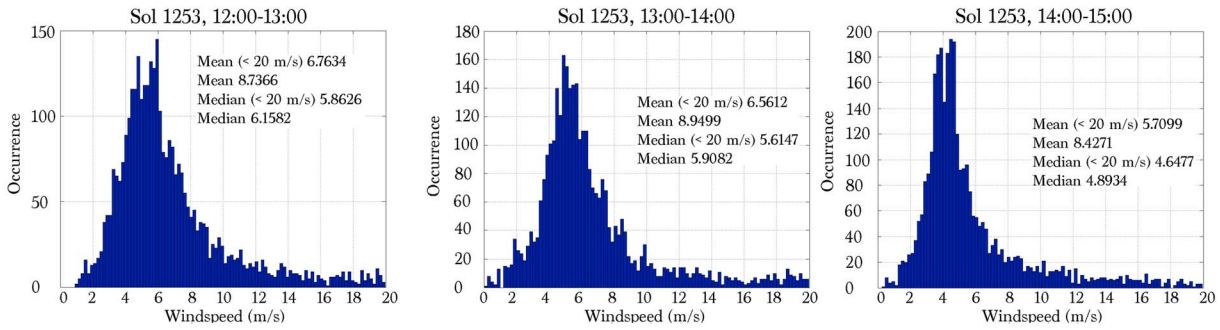

Figure 16. All of the 14:00–16:00 REMS filtered 1 Hz results that occurred while *Curiosity* was at the dump piles.

4. Discussion

4.1. Mobility of Martian Sand in a Low Wind Season

The results from MarsWRF, orbital HiRISE tracking, and the Curiosity rover consistently show that the Bagnold Dune Campaign occurred in the period of lowest aeolian activity during the Martian year. The MarsWRF maximum predicted wind speeds at 1.5 m during the L_s range of the Bagnold campaign are predicted to be ~4–8 m s^{-1} (Figure 4, top left). The measured mean wind speeds for hours 11:00–12:00 and 14:00–16:00 sampled by REMS during the campaign are 5–9 or 3–7 m s^{-1}, depending on whether values above 20 m s^{-1} are included or not, respectively, in the average. These two data sets therefore show fairly good agreement and are consistent with the very limited dune ripple displacement seen with HiRISE. These values can be converted to friction speeds to compare to predictions for the sand motion threshold on Mars. Assuming a range of roughness heights (z_0) of 10–100 μm, a 1.5 m wind speed of 3–9 m s^{-1} converts to friction speeds of ~0.1–0.3 m s^{-1} (equation (1)). This is about an order of magnitude below the predicted fluid threshold for basalt particles on Mars but above the impact threshold for fine sand (Figure 1). The REMS 1 Hz plots clearly show a tail going up to the calibration limit of 20 m s^{-1}. This converts to a friction speed of ~0.7–0.8 m s^{-1}, a value still well below the fluid threshold for basalt particles but comparable to the threshold value (~0.8 ms^{-1}) needed to reconcile MarsWRF and seasonal sand flux variations measured from HiRISE [*Ayoub et al.*, 2014]. We can also consider whether the moving grains are composed of material of lower density than basalt. In many of our observations bright grains seemed to move more readily than darker grains, although this could be an observational bias. Calcium sulfate veins are common in Gale Crater [*Nachon et al.*, 2014] and are found in bedrock among the Bagnold Dunes. Detailed ChemCam analysis indicates that bassanite ($CaSO_4{\cdot}0.5H_2O$) is the most likely composition [*Rapin et al.*, 2016]. With a lower density, at ~2730 km m $^{-3}$, than typical basalt at 3000 kg m^{-3}, it will have only a slightly lower threshold (Figure 1b).

Therefore, taken at face value, the REMS and MarsWRF results predict that sand should never be mobilized during the period of the Bagnold Dune Campaign. However, as we have shown, there is at least some wind-related surface activity seen by Curiosity's cameras and HiRISE, and - as evinced by the intrasol changes detected - at least some of it occurs during the warmer periods when wind speeds could be measured by REMS. Three explanations are likely. First, the REMS 1 Hz wind data have an asymmetric distribution that peaks at lower wind speed, with a decreasing tail extending to higher values. This type of wind speed frequency distribution is typical of many windy environments and is commonly described utilizing a Weibull distribution function [*Seguro and Lambert*, 2000], which has been applied to Viking Lander 2 wind speed measurements [*Lorenz*, 1996]:

$$f(u) = (k/c)(u/c)^{k-1} \exp\left(-[u/c]^k\right) \tag{3}$$

where u is the wind speed, c is the scale speed, and k is a dimensionless curve shape parameter >1 that is proportional to the gustiness, and therefore the shallowness of the high-speed tail. Initial examination of REMS data by *Viudez-Moreiras et al.* [2017] shows that the high-frequency REMS wind data can be described using a Weibull function. For REMS data examined by *Viudez-Moreiras et al.* [2017], values of c = 5.496 m s^{-1} and k = 1.828 fit the data well. Such a distribution predicts just 0.002% of winds above 20 m s^{-1}. If the distribution is more akin to that found in windy periods of the Viking Lander 2 mission in which c = 7.45 m s^{-1} and k = 1.48 [*Lorenz*, 1996], then 1.4% of winds are above 20 m s^{-1} and 0.04% above 30 m s^{-1}. Note that the increase in the parameter c moves the center of the distribution to higher values, and as described above, peak activity in the Namib lee region may have been coincident with the highest mean wind speeds from 11:00–12:00, 14:00–16:00 measured by REMS in this area. These REMS results are shown compared to the *Lorenz* Viking Lander 2 Weibull distribution in Figure 17. Although fitting the REMS records to distribution curves is an ongoing study and beyond the scope of this paper, these comparisons show that short-term gusts may affect loose surface particles even during seasons when overall wind activity is low.

The second explanation is that thresholds computed and measured in the wind tunnel may not be applicable to the changes observed during the Bagnold Dune Campaign. Most wind tunnel and theoretical treatments focus on the conditions needed to detach a particle from the surface and loft it either by suspension (if small and low density) or saltation (if larger and denser; this applies to fine sand sizes and larger). More recent wind tunnel tests and modeling show that detachment of Mars analog materials by rolling can occur at shear stresses less than half that needed for traditional fluid threshold [*Merrison et al.*, 2007; *de Vet et al.*, 2014]. Similarly, in terrestrial wind tunnels it has been shown that clasts undergo distinct stages of threshold, starting

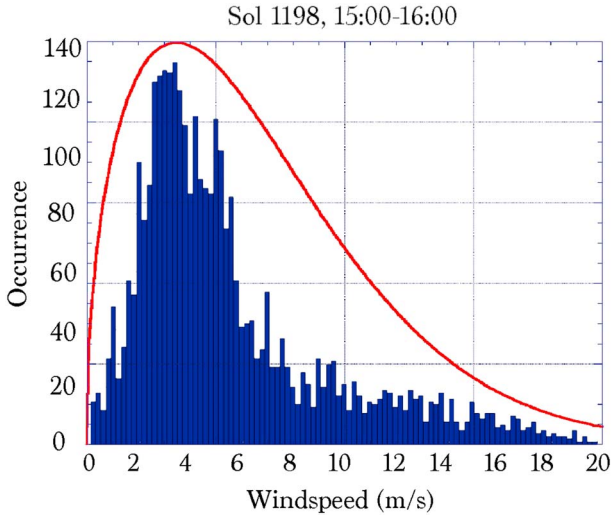

Figure 17. An example of a Weibull distribution curve overlaid on REMS filtered 1 Hz data on sol 1198, 15:00–16:00 LMST. Weibull parameters *c* and *k* are chosen as 7.45 m s^{-1} and 1.48, respectively, values that match wind speeds measured by Viking Lander 2 [*Lorenz*, 1996], but do not match these REMS data well. This 1 h period had the second highest median wind speed (both using all sampled data and those only below 20 m s^{-1}) and the third highest mean speed for 11:00–12:00, 14:00–16:00 EB results at Namib dune and occurred during an imaging sol interval from 1198 to 1200 when more changes were seen (see text).

with vibrating, then transitioning to intermediate sliding and rolling (depending on the substrate), and concluding with detachment. In these studies, the vibration threshold was measured at about 50–60% of that at saltation [*Bridges et al.*, 2015]. It is very likely that the particle movement observed in this low wind period which overlapped with the Bagnold Dune Campaign was from such intermediate stage processes.

Finally, in a windy environment, any exposed sand will continue to get blown until it reaches a sheltered location. This "survival of the fittest" evolutionary process results in the concentration of sand where it is protected by the local roughness and sheltered in topographic lows. When sand is freshly exposed and unconsolidated, it is more likely to become entrained by the wind. This explains the changes seen within a single sol on the dump piles and the grain scrambling in sandy areas freshly disturbed by the rover wheels. Production of unconsolidated sand can occur due to several mechanisms. One is wind gusts that may just saltate a few grains of sand that, when they impact a sand bed, splash more grains. Such short-lived occurrences can deposit fresh sand on rock faces and other exposed locations. Other processes also act to alter the Martian regolith. Diurnal temperature changes in Gale Crater are on the order of 90 K [*Hamilton et al.*, 2014; *Martinez et al.*, 2016], significantly greater than any geologic setting on Earth. Thermal expansion and contraction of sand grains may act to destabilize metastable slopes or push grains up where they are more exposed to local wind flow. Although nighttime frost has not been directly detected in Gale and daytime DAN measurements show the lowest subsurface hydrogen content so far measured in the mission [*Ehlmann et al.*, 2017], the Bagnold Dune Campaign occurred during the coldest part of the Martian year when it is predicted that nighttime frost of a few microns in thickness could form [*Martinez et al.*, 2016]. As with diurnal temperature changes, daily displacements in volume may occur as the frost condenses within porous spaces between grains, and perhaps alters interparticle forces. Although all of these processes are subtle, they may be influential in a low aeolian activity environment in which short wind gusts will exploit whatever exposed sand is available.

4.2. Inferred Threshold Limits on Mars

Because the 1 Hz resolution of REMS cannot be matched by a similar imaging frequency, to gauge threshold we are limited to wind distributions over time periods bookended by images showing changes. However, as we have shown, many changes cannot be constrained to a single sol and in other instances no grain scrambling occurred despite a wide distribution of wind speeds. Nevertheless, in two cases, at Solitaire and at the dump piles, intrasol changes were observed when mean wind speeds exceeded 8.5 m s^{-1}, a measured mean condition only exceeded in one other EB examined (1239, 15:00–16:00; Table 4b). Assuming a standard wind speed distribution, it may be that such mean values are generally representative of when changes are likely to occur. Taking a roughness height of 10–100 μm and the REMS height of 1.5 m, this correlates to a mean friction speed of 0.3–0.4 m s^{-1}. Similarly, what processes *did not* occur are as significant as those that did. Whereas grain scrambling can be attributed to surface particle rolling and sliding, or perhaps limited saltation in gusts, and other processes such as grain flow to non-aeolian effects, the movement of ripples would provide strong evidence of sustained saltation, yet this was not observed. Therefore, considering the REMS results combined with this negative outcome, average winds above ~8–10 m s^{-1} are probably needed for such activity to occur (Figures 7 and 8 and Tables 4a and 4b).

4.3. Implication for Mars Aeolian Processes and Geology

The record of aeolian activity on Mars continues to grow with the acquisition of new data. Whereas many initial studies of dune and ripple migration focused on integrated changes over long temporal baselines [*Bridges et al.*, 2013], only recently has the ability to conduct seasonal studies at high temporal resolution from orbit been achieved [*Ayoub et al.*, 2014]. Because the timing of *Curiosity*'s visit to the Bagnold Dunes could not be chosen a priori, the resulting aeolian part of the campaign occurred when wind activity was very limited. Nevertheless, the lessons learned have broad applicability for Mars, and the measurements made can be used as a guide for processes that are likely occurring today elsewhere on the planet, as well as in the past.

All of Mars undergoes seasonal cycles. With orbital studies of sand migration achieved at Nili Patera and now Gale, with the latter augmented by ground truth measurements, and in comparing to the MarsWRF results, it seems that the period centered on the southern winter/northern summer solstice is a time of relative aeolian quiescence at the Bagnold Dunes. The changes that do occur, as described in this paper, are limited to movement of ripples on the upper surfaces of dunes (as seen in HiRISE over many months) and, at the surface-dune interface (viewed by *Curiosity*), limited episodes of grain movement and occasional grain flows. These events are likely driven by rare gusts that may be augmented with other non-aeolian triggering mechanisms. It is only as the season changes that these limited processes become overwhelmed by more extensive ripple and dune migration activity.

The Martian climate has changed over time. Evidence for significant volumes of flowing and standing bodies of water in the Noachian and Hesperian eras (4.1–3 Ga) points to past conditions when the atmosphere was probably thicker and the temperature maybe warmer [*Bibring et al.*, 2006; *Grotzinger et al.*, 2011]. However, bedforms present on the surface are affected by more recent climatic fluctuations under dry conditions. Mars is subjected to large changes in obliquity, precession, and eccentricity, parameters that affect solar insolation as a function of latitude and season [*Laskar et al.*, 2004]. Variations in precession and eccentricity can change the magnitude of near-surface winds [*Haberle et al.*, 2003]. Considering these changing conditions, it is reasonable to consider whether bedform motion and associated geomorphic processes are cyclical at geologic (non annual) time scales. A related question is the magnitude of current processes. If moderate to major, then lulls in the climate cycles are an appealing mechanism for lowering the activity of dunes and ripples. As obliquity decreases, so does mean wind stress [*Haberle et al.*, 2003]. That, combined with a decrease in atmospheric pressure and resulting decrease in wind stress, indicates that some past Martian climates were, for a greater fraction of a given year, analogous to the low activity conditions documented in this paper. In such periods, it is likely that many dunes become inactive and more prone to becoming permanently stalled as processes that promote sand induration, such as dust infiltration and cementation by Cl- and S-rich salts mobilized by water vapor diffusion [*Jakosky and Christensen*, 1986], dominate over wind. The period investigated in the Bagnold Dune Campaign is not at this end state, as the local dunes are active currently, albeit mostly in a different season, and thereby provide loose sand for the observed processes to take place. Rather, the processes reported here represent an intermediate stage between high and low activities that bridge, to varying degrees, climatic states in Mars' recent past. These results should therefore be considered when gauging aeolian processes from the Martian rock record or models of its geologic history.

Acknowledgments

Reviews by Paul Geissler and an anonymous reviewer improved this paper. We thank Jasper Kok for providing the impact threshold calculations in Figure 1. We acknowledge Matthew Chojnacki and the University of Arizona/HiRISE Operations Center who produced the stereo-derived *T9*/*S1*-2 (Table 1) digital elevation model. We are grateful to Tim Parker for helping generate the rover traverse map seen in Figure 2. Great appreciation is extended to the Mars Science Laboratory Project for the time and effort they extended in conducting the Bagnold Dune Campaign. Funding for this work in the U.S. was provided by the Mars Exploration Program to the MSL Project and, for HiRISE studies by the first author, the MRO Project and the Mars Data Analysis Program. S. Silvestro was supported by ASI through the ASI-CISAS agreement I/018/ 12/0: "DREAMS EDM Payload—ExoMars 2016". MarsWRF simulations were performed on NASA's HEC Pleiades cluster and partly supported by the Mars Fundamental Research Program. Additional data discussed in this paper that are not included in the text, tables, figures, or supporting information may be requested from the corresponding author, Claire Newman (claire@aeolisresearch.com).

References

Achilles, C. A., et al. (2017), Mineralogy of an active eolian sediment from the Namib Dune, Gale Crater, Mars, *J. Geophys. Res. Planets*, *122*, doi:10.1002/2017JE005262.

Almeida, M. P., E. J. R. Parteli, J. S. Andrade, and H. J. Herrmann (2008), Giant saltation on Mars, *Proc. Natl. Acad. Sci. U.S.A.*, *105*, 6222–6226.

Anderson, R. S. (1987), A theoretical model for aeolian impact ripples, *Sedimentology*, *34*, 943–956.

Andreotti, B. (2004), A two-species model of aeolian sand transport, *J. Fluid Mech.*, *510*, 47–70.

Avouac, J. P., F. Ayoub, S. Leprince, O. Konca, and D. Helmberger (2006), The 2005, M_w 7.6 Kashmir earthquake, rupture kinematics from sub-pixel correlation of ASTER images and seismic waveforms analysis, *Earth Planet. Sci. Lett.*, *249*, 514–528.

Ayoub, F., J.-P. Avouac, C. E. Newman, M. I. Richardson, A. Lucas, S. Leprince, and N. T. Bridges (2014), Threshold for sand mobility on Mars calibrated from seasonal variations in sand flux, *Nature Comm.*, *5*, 5096, doi:10.1038/ncomms6096.

Ayoub, F., S. Leprince, and J.-P. Avouac (2015), *User's Guide to COSI-CORR Co-Registration of Optically Sensed Images and Correlation*, 49 pp., Calif. Inst. Technol. [Available at http://www.tectonics.caltech.edu/slip_history/spot_coseis/pdf_files/CosiCorr-Guide2015a.pdf.]

Bagnold, R. A. (1941), *The Physics of Blown Sand and Desert Dunes*, Methuen, London.

Bibring, J. P., et al. (2006), Global mineralogical and aqueous Mars history derived from OMEGA/Mars Express data, *Science*, *312*, 400–404.

Bridges, N. T., and B. L. Ehlmann (2017), The Mars Science Laboratory (MSL) Bagnold Dunes campaign, Phase I: Overview and introduction to the special issue, *J. Geophys. Res. Planets*, *122*, doi:10.1002/2017JE005401.

Bridges, N. T., P. E. Geissler, A. S. McEwen, B. J. Thomson, F. C. Chuang, K. E. Herkenhoff, L. P. Keszthelyi, and S. Martínez-Alonso (2007), Windy Mars: A dynamic planet as seen by the HiRISE camera, *Geophys. Res. Lett.*, *34*, L23205, doi:10.1029/2007GL031445.
Bridges, N. T., et al. (2012a), Planet-wide sand motion on Mars, *Geology*, *40*, 31–34.
Bridges, N. T., F. Ayoub, J.-P. Avouac, S. Leprince, A. Lucas, and S. Mattson (2012b), Earth-like sand fluxes on Mars, *Nature*, *485*, 339–342.
Bridges, N. T., P. Geissler, S. Silvestro, and M. Banks (2013), Bedform migration on Mars: Current results and future plans, *Aeolian Res.*, *9*, 133–151, doi:10.1016/j.aeolia.2013.02.004.
Bridges, N. T., M. G. Spagnuolo, S. L. de Silva, J. R. Zimbelman, and E. M. Neely (2015), Formation of gravel-mantled megaripples on Earth and Mars: Insights from the Argentinean Puna and wind tunnel experiments, *Aeolian Res.*, *17*, 49–60.
Cardinale, M., S. Silvestro, D. A. Vaz, T. Michaels, M. C. Bourke, G. Komatsu, and L. Marinangeil (2016), Present-day aeolian activity in Herschel Crater, Mars, *Icarus*, *265*, 139–148.
Chojnacki, D., D. M. Burr, J. E. Moersch, and J. J. Wray (2014), Valles Marineris dune sediment provenance and pathways, *Icarus*, *232*, 187–219.
Chojnacki, M., D. M. Burr, J. E. Moersch, and T. J. Michaels (2011), Orbital observations of contemporary dune activity in Endeavour Crater, Meridiani Planum, Mars, *J. Geophys. Res.*, *116*, E00F19, doi:10.1029/2010JE003675.
Chojnacki, M., J. R. Johnson, J. E. Moersch, L. K. Fenton, T. I. Michaels, and J. F. Bell (2015), Persistent aeolian activity at Endeavour crater, Meridiani Planum, Mars; new observations from orbit and the surface, *Icarus*, *251*, 275–290.
Christensen, P. R., et al. (2001), Mars Global Surveyor Thermal Emission Spectrometer experiment: Investigation description and surface science results, *J. Geophys. Res.*, *106*, 23,823–23,871.
Claudin, P., and B. Andreotti (2006), A scaling law for aeolian dunes on Mars, Venus, Earth, and for subaqueous ripples, *Earth Planet. Sci. Lett.*, *252*, 30–44.
Cousin, A., et al. (2017), Geochemistry of the Bagnold Dune Field as observed by ChemCam, and comparison with other aeolian deposits at Gale Crater, *J. Geophys. Res. Planets*, *122*, doi:10.1002/2017JE005261.
Day, M., and G. Kocurek (2016), Observations of an aeolian landscape: From surface to orbit in Gale Crater, *Icarus*, *280*, 37–71.
de Vet, S. J., J. P. Merrison, M. C. Mittelmeijer-Hazeleger, E. E. van Loon, and L. H. Cammeraat (2014), Effects of rolling on wind-induced detachment thresholds of volcanic glass on Mars, *Planet. Space Sci.*, *103*, 205–218.
Edgett, K. S., et al. (2012), Curiosity's Mars Hand Lens Imager (MAHLI) investigation, *Space Sci. Rev.*, *170*, 259–317, doi:10.1007/s11214-012-9910-4.
Ehlmann, B. L., et al. (2017), Chemistry, mineralogy, and grain properties at Namib and High Dunes, Bagnold Dune Field, Gale Crater, Mars: A synthesis of Curiosity Rover observations, *J. Geophys. Res. Planets*, *122*, doi:10.1002/2017JE005267.
Ewing, R. C., et al. (2017), Sedimentary structures of the Bagnold Dunes: Implications for eolian rock record of Mars, *J. Geophys. Res. Planets*, *122*, doi:10.1002/2017JE005324.
Fenton, L. K., T. I. Michaels, and M. Chojnacki (2014a), Late Amazonian aeolian features, gradation, wind regimes, and sediment state in the vicinity of the Mars Exploration Rover Opportunity, Meridiani Planum, Mars, *Aeolian Res.*, *16*, 75–99.
Fenton, L. K., T. I. Michaels, and R. A. Beyer (2014b), Inverse maximum gross bedform-normal transport 1: How to determine a dune-constructing wind regime using only imagery, *Icarus*, *230*, 5–14.
Fryberger, S. G., and G. Dean (1979), Dune forms and wind regime, in *A Study of Global Sand Seas*, *U.S. Geol. Surv. Prof. Pap., 1052*, edited by E. D. McKee, pp. 137–170, U.S. Gov. Print. Off., Washington, D. C.
Geissler, P. E., N. W. Stantzos, N. T. Bridges, M. C. Bourke, S. Silvestro, and L. K. Fenton (2013), Shifting sand on Mars: Insights from tropical intra-crater dunes, *Earth Surf. Processes Landforms*, *48*, 407–412.
Gómez-Elvira, J., et al. (2012), REMS: The environmental sensor suite for the Mars Science Laboratory rover, *Space Sci. Rev.*, *170*, 583–640, doi:10.1007/s11214-012-9921-1.
Gómez-Elvira, J., et al. (2014), Curiosity's Rover Environmental Monitoring Station: Overview of the first 100 sols, *J. Geophys. Res. Planets*, *119*, 1680–1688, doi:10.1002/2013JE004576.
Greeley, R., and J. D. Iversen (1985), *Wind as a Geological Process on Earth, Mars, Venus, and Titan*, Cambridge Univ. Press, Cambridge.
Greeley, R., J. D. Iversen, J. B. Pollack, N. Udovich, and B. White (1974), Wind-tunnel studies of Martian aeolian processes, *Proc. R. Soc. London, Ser. A*, *341*, 331.
Grotzinger, J., et al. (2011), Mars sedimentary geology: Key concepts and outstanding questions, *Astrobiology*, *11*, 77–87.
Grotzinger, J. P., J. A. Crisp, and A. R. Vasavada (2015), Curiosity's mission of exploration at Gale Crater, Mars, *Elements*, *11*, 19–26.
Haberle, R. M., J. R. Murphy, and J. Schaeffer (2003), Orbital change experiments with a Mars general circulation model, *Icarus*, *161*, 66–89.
Hamilton, V. E., et al. (2014), Observations and preliminary science results from the first 100 sols of MSL REMS ground temperature sensor measurements at Gale Crater, *J. Geophys. Res. Planets*, *119*, 745–770, doi:10.1029/2013JE004520.
Hayward, R. K., K. F. Mullins, L. K. Fenton, T. M. Hare, T. N. Titus, M. C. Bourke, A. Colaprete, and P. R. Christensen (2007), Mars global digital dune database and initial science results, *J. Geophys. Res.*, *112*, E11007, doi:10.1029/2007JE002943.
Hansen, C. J., et al. (2011), Seasonal erosion and restoration of Mars' northern polar dunes, *Science*, *331*, 575–578.
Iversen, J. D., and B. R. White (1982), Saltation threshold on Earth, Mars, and Venus, *Sedimentology*, *29*, 111–119.
Iversen, J. D., J. B. Pollack, R. Greeley, and B. R. White (1976), Saltation threshold on Mars: The effect of interparticle force, surface roughness, and low atmospheric density, *Icarus*, *29*, 381–393.
Jakosky, B. M., and P. R. Christensen (1986), Global duricrust on Mars—Analysis of remote-sensing data, *J. Geophys. Res.*, *91*, 3547–3559.
Kirk, R. L., et al. (2008), Ultrahigh resolution topographic mapping of Mars with MRO HiRISE stereo images: Meter-scale slopes of candidate Phoenix landing sites, *J. Geophys. Res.*, *113*, E00A24, doi:10.1029/2007JE003000.
Kok, J. F. (2010a), An improved parameterization of wind-blown sand flux on Mars that includes the effect of hysteresis, *Geophys. Res. Lett.*, *37*, L12202, doi:10.1029/2010GL043646.
Kok, J. F. (2010b), Difference in the wind speeds required for initial versus continuation of sand transport on Mars: Implications for dunes and dust storms, *Phys. Rev. Lett.*, *104*, 074502, doi:10.1103/PhysRevLett.104.074502.
Kok, J. F., and N. O. Renno (2009), A comprehensive numerical model of steady state saltation (COMSALT), *J. Geophys. Res.*, *114*, D17204, doi:10.1029/2009JD011702.
Kok, J. F., E. J. R. Parteli, T. I. Michaels, and D. Bou Karam (2012), The physics of wind-blown sand and dust, *Rep. Prog. Phys.*, *75*, 106901.
Lapotre, M., et al. (2016), Large wind ripples on Mars: A record of atmospheric evolution, *Science*, *353*, 55–58.
Lapotre, M. G. A., B. L. Ehlmann, S. E. Minson, R. E. Arvidson, F. Ayoub, A. A. Fraeman, R. C. Ewing, and N. T. Bridges (2017), Compositional variations in sands of the Bagnold Dunes, Gale Crater, Mars, from visible-shortwave infrared spectroscopy and comparison with ground truth from the Curiosity rover, *J. Geophys. Res. Planets*, *122*, doi:10.1002/2016JE005133.
Laskar, J., A. C. M. Correia, M. Gastineau, F. Joutel, B. Levrard, and P. Robutel (2004), Long term evolution and chaotic diffusion of the insolation quantities of Mars, *Icarus*, *170*, 343–364.

Le Mouélic, S., et al. (2015), The ChemCam Remote Micro-Imager at Gale Crater: Review of the first year of operations at Mars, *Icarus*, *249*, 93–107.
Leprince, S., S. Barbot, F. Ayoub, and J. P. Avouac (2007), Automatic, precise, ortho-rectification and co-registration for satellite image correlation, application to Seismotectonics, *IEEE Trans. Geosci. Remote Sens.*, *45*, 1529–1558.
Lorenz, R. D. (1996), Martian surface windspeeds, described by the Weibull distribution, *J. Spacecr. Rockets*, *33*, 754–756.
Mahaffy, P. R., et al. (2012), The sample analysis at Mars investigation and instrument suite, *Space Sci. Rev.*, *170*(1–4), 401–478.
Malin, M. C., et al. (2010), The Mars Science Laboratory (MSL) Mast-Mounted Cameras (Mastcams) flight instruments, *Proc. Lunar Planet. Sci. Conf. 41st*, Abstract 1123.
Martinez, G. M., et al. (2016), Likely frost events at Gale Crater: Analysis from MSL/REMS measurements, *Icarus*, *280*, 93–102.
Maurice, S., et al. (2012), The ChemCam instrument suite the Mars Science Laboratory (MSL) rover: Science objectives and mast unit description, *Space Sci. Rev.*, *170*, 95–166, doi:10.1007/s11214-012-9912-2.
Mayaud, J. R., R. M. Bailer, G. F. S. Wiggs, and C. M. Weaver (2017), Modeling aeolian sand transport using a dynamic mass balancing approach, *Geomorphology*, *280*, 108–121.
McEwen, A. S., et al. (2007), Mars Reconnaissance Orbiter's High Resolution Imaging Science Experiment (HiRISE), *J. Geophys. Res.*, *112*, E05S02, doi:10.1029/2005JE002605.
Merrison, J. P., H. P. Gunnlaugsson, P. Nørnberg, A. E. Jensen, and K. R. Rasmussen (2007), Determination of the wind induced detachment threshold for granular material on Mars using wind tunnel simulation, *Icarus*, *91*, 568–580.
Mitrofanov, I. G., et al. (2012), Dynamic Albedo of Neutrons (DAN) experiment onboard NASA's Mars Science Laboratory, *Space Sci. Rev.*, *170*, 559–582, doi:10.1007/s11214-012-9924-y.
Nachon, M., et al. (2014), Calcium sulfate veins characterized by ChemCam/Curiosity at Gale Crater, Mars, *J. Geophys. Res. Planets*, *119*, 1991–2016, doi:10.1002/2013JE004588.
Necsoiu, M., S. Leprince, D. M. Hooper, C. L. Dinwiddie, R. N. McGinnis, and G. R. Walter (2009), Monitoring migration rates of an active subarctic dune field using optical imagery, *Remote Sens. Environ.*, *113*, 2441–2447.
Newman, C. E., and M. I. Richardson (2015), The impact of surface dust source exhaustion on the Martian dust cycle, dust storms and interannual variability, as simulated by the MarsWRF general circulation model, *Icarus*, *257*, 47–87.
Newman, C. E., et al. (2017), Winds measured by the Rover Environmental Monitoring Stations (REMS) during Mars Science Laboratory (MSL) rover's Bagnold Dunes Campaign and comparison with numerical modeling using MarsWRF, *Icarus*, *291*, 203–231, doi:10.1016/j.icarus.2016.12.016.
O'Connell-Cooper, C., et al. (2017), Geochemistry of the Bagnold Dune Sands, as analyzed by APXS, and comparison to other soils within Gale Crater, and to a global Martian average, *J. Geophys. Res. Planets*, *122*, doi:10.1002/2017JE005268.
Ould Ahmedou, D., A. Ould Mahfoudh, P. Dupont, A. Ould El Moctar, A. Valance, and K. R. Rasmussen (2007), Barchan dune mobility in Mauritania related to dune and interdune fluxes, *J. Geophys. Res.*, *112*, F02016, doi:10.1029/2006JF000500.
Prandtl, L. (1935), The mechanics of viscous flows, in *Aerodynamic Theory*, vol. III, edited by W. F. Durand, pp. 34–208, Springer, Berlin.
Rapin, W., et al. (2016), Hydration state of calcium sulfates in Gale Crater, Mars: Identification of bassanite veins, *Earth Planet. Sci. Lett.*, *452*, 197–205.
Richardson, M. I., A. D. Toigo, and C. E. Newman (2007), PlanetWRF: A general purpose, local to global numerical model for planetary atmospheric and climate dynamics, *J. Geophys. Res.*, *112*, E09001, doi:10.1029/2006JE002825.
Runyon, K. D., N. T. Bridges, F. Ayoub, C. E. Newman, and J. J. Quade (2017), An integrated model for dune morphology and sand fluxes on Mars, *Earth Planet. Sci. Lett.*, *257*, 204–212.
Seguro, J. V., and T. W. Lambert (2000), Modern estimation of the parameters of the Weibull wind speed distribution for wind energy analysis, *J. Wind Eng. Ind. Aerodyn.*, *85*, 75–84.
Silvestro, S., L. K. Fenton, D. A. Vaz, N. T. Bridges, and G. G. Ori (2010), Ripple migration and dune activity on Mars: Evidence for dynamic processes, *Geophys. Res. Lett.*, *37*, L20203, doi:10.1029/2010GL044743.
Silvestro, S., D. A. Vaz, L. K. Fenton, and P. E. Geissler (2011), Active aeolian processes on Mars: A regional study in Arabia and Meridiani Terrae, *Geophys. Res. Lett.*, *38*, L20201, doi:10.1029/2011GL048955.
Silvestro, S., D. A. Vaz, R. C. Ewing, A. P. Rossi, L. K. Fenton, T. I. Michaels, J. Flahaut, and P. E. Geissler (2013), Pervasive aeolian activity along rover Curiosity's traverse in Gale Crater, Mars, *Geology*, *41*, 483–486, doi:10.1130/G34162.1.
Silvestro, S., D. A. Vaz, H. Yizhaq, and F. Esposito (2016), Dune-like dynamic of Martian aeolian large ripples, *Geophys. Res. Lett.*, *43*, 8384–8389, doi:10.1002/2016GL070014.
Smith, D. E., et al. (2001), Mars Orbiter Laser Altimeter: Experiment summary after the first year of global mapping of Mars, *J. Geophys. Res.*, *106*, 23,689–23,722.
Sullivan, R., and J. Kok (2017), Aeolian saltation on Mars at low to moderate wind speeds, *J. Geophys. Res. Planets*, *122*, doi:10.1002/2017JE005275.
Sullivan, R., et al. (2008), Wind-driven particle mobility on Mars: Insights from MER observations at "El Dorado" and surroundings at Gusev Crater, *J. Geophys. Res.*, *113*, E06S07, doi:10.1029/2008JE003101.
Toigo, A. D., C. Lee, C. E. Newman, and M. I. Richardson (2012), The impact of resolution on the dynamics of the Martian global atmosphere: Varying resolution studies with the MarsWRF GCM, *Icarus*, *221*, 267–288.
Tsoar, H. (2001), Types of aeolian sand dunes and their formation, in *Geomorphological Fluid Mechanics*, edited by N. J. Balmforth and A. Provenzale, pp. 403–429, Springer, Berlin.
Vaz, D. A., and S. Silvestro (2014), Mapping and characterization of small-scale aeolian structures on Mars: An example from the MSL landing site in Gale Crater, *Icarus*, *230*, 151–161, doi:10.1016/j.icarus.2013.08.007.
Vermeesch, P., and N. Drake (2008), Remotely sensed dune celerity and sand flux measurements of the world's fastest barchans (Bodele, Chad), *Geophys. Res. Lett.*, *35*, L24404, doi:10.1029/2008GL035921.
Viudez-Moreiras, D., J. Gómez-Elvira, C. E. Newman, S. Navarro, M. Marian, and the REMS Team (2017), Gale wind speed Weibull distribution based on the first two years of REMS wind data, *6th Inter. Conf. Mars Atmosphere*, Granada, Spain.
White, B. R. (1979), Soil transport by winds on Mars, *J. Geophys. Res.*, *84*, 4643–4651.
White, B. R. (1986), Particle dynamics in two-phase flows, in *Encyclopedia of Fluid Mechanics*, chap. 8, pp. 239–282, Gulf, Houston, Tex.
White, B. R., R. Greeley, J. D. Iversen, and J. B. Pollack (1976), Estimated grain saltation in a Martian atmosphere, *J. Geophys. Res.*, *81*(32), 5643–5650, doi:10.1029/JB081i032p05643.
Yingst, R. A., et al. (2016), Characteristics of pebble and cobble-sized clasts along Curiosity traverse from sol 100 to 750: Terrain types, potential sources, and transport mechanisms, *Icarus*, *280*, 72–92.